bioRxiv preprint doi: https://doi.org/10.1101/2020.12.17.423349; this version posted December 20, 2020. The copyright holder for this preprint (which was not certified by peer review) is the author/funder, who has granted bioRxiv a license to display the preprint in perpetuity. It is made available under aCC-BY-NC-ND 4.0 International license.

Recovery of neural dynamics criticality in personalized whole brain models of stroke

Rodrigo P. Rocha[1,2,3,†], Loren Koçillari[3,4], Samir Suweis[3,5], Michele De Filippo De Grazia[6], Michel Thiebaut de Schotten[7,8], Marco Zorzi[6,9], and Maurizio Corbetta[3,10,11]

[1]Departamento de Física, Centro de Ciências Físicas e Matemáticas, Universidade Federal de Santa Catarina, 88040-900, Florianópolis, SC, Brazil.
[2]Department of Physics, School of Philosophy, Sciences and Letters of Ribeirão Preto, University of São Paulo, Ribeirão Preto, SP, Brazil.
[3]Padova Neuroscience Center, Università di Padova, Padova, Italy.
[4]Laboratory of Neural Computation, Istituto Italiano di Tecnologia, 38068 Rovereto, Italy.
[5]Dipartimento di Fisica e Astronomia, Università di Padova and INFN, via Marzolo 8, I-35131 Padova, Italy.
[6]Fondazione Ospedale San Camillo IRCCS, Venezia, Italy.
[7]Brain Connectivity and Behaviour Laboratory, BCBlab, Sorbonne Universities, Paris France.
[8]Groupe d'Imagerie Neurofonctionnelle, Institut des Maladies Neurodégénératives-UMR 5293, CNRS, CEA University of Bordeaux, Bordeaux, France.
[9]Dipartimento di Psicologia Generale, Università di Padova, Padova, Italy.
[10]Dipartimento di Neuroscienze, Università di Padova, Padova, Italy.
[11]Venetian Institute of Molecular Medicine (VIMM), Fondazione Biomedica, Padova
[†]Correspondence to rodrigo.rocha@ufsc.br

ABSTRACT

The critical brain hypothesis states that biological neuronal networks, because of their structural and functional architecture, work near phase transitions for optimal response to internal and external inputs. Criticality thus provides optimal function and behavioral capabilities. We test this hypothesis by examining the influence of brain injury (strokes) on the criticality of neural dynamics estimated at the level of single subjects using whole-brain models. Lesions engendered a sub-critical state that recovered over time in parallel with behavior. Notably, this improvement of criticality depended on the re-modeling of specific white matter connections. In summary, personalized whole-brain dynamical models poised at criticality track neural dynamics, alteration post-stroke, and behavior at the level of single subjects.

Introduction

The fundamental mechanisms underlying the dynamics of brain activity are still largely unknown. Interdisciplinary neuroscience research, inspired by statistical physics, has suggested that healthy brain's neural dynamics stay close to a critical state[1], i.e., in the vicinity of a critical phase transition between order and disorder[2,3], or between asynchronous or synchronous oscillatory activity[4,5]. In physics, critical phenomena occur at the transition of different states of the systems (also known as phase transitions) for specific values of the so-called system's control parameter (e.g., temperature). There is mounting evidence that biological systems (or parts, aspects, or groups) operate near/at critical points[6,7]. Examples include gene expression patterns[8], bacterial clustering[9], flock dynamics[10], as well as spontaneous brain activity. Indeed, neural systems seem to display features that are characteristic of systems at criticality. These include i) the scaling invariance of neural avalanches[5,11] reported in diverse species[12,13], through different imaging techniques[14], and electro-physiological signals[15]; ii) the presence of long-range spatiotemporal correlations in the amplitude fluctuations of neural oscillations[16,17], including the observation of $1/f$ power spectra from simultaneously recorded MEG/EEG signals[15], fMRI[18], and cognitive responses[19].

Critical brains benefit from these emergent features to promptly react to external stimuli to maximize information transmission[20], hence sensitivity to sensory stimuli, storage of information[21], and a coordinated global behavior[11,22]. If criticality is indeed a fundamental property of healthy brains[2], then neurological dysfunctions shall alter this optimal dynamical configuration. However, we know little about the effect of brain disorders on criticality[23]. Some studies have reported disrupted criticality during epileptic seizures[24,25], slow-wave sleep[26], anesthesia[27], sustained wakefulness[28], states of (un)consciousness[29,30], and Alzheimer's disease[31]. However, a crucial test of the hypothesis requires showing alterations of criticality after focal brain injuries that cause local alterations of the brain's structural and functional architecture. If criticality is essential for behavior,

bioRxiv preprint doi: https://doi.org/10.1101/2020.12.17.423349; this version posted December 20, 2020. The copyright holder for this preprint (which was not certified by peer review) is the author/funder, who has granted bioRxiv a license to display the preprint in perpetuity. It is made available under aCC-BY-NC-ND 4.0 International license.

then its alteration after focal injury shall relate to behavioral dysfunction. Over time as behavior improves in the course of recovery, so shall criticality. Finally, changes in criticality with recovery will depend on specific plasticity mechanisms or functional remodeling as shown in previous work[32,33]. Here we use stroke as the prototypical pathological model of human focal brain injury and whole-brain computational models to estimate neural dynamics, related alterations in criticality and behavior, and the underlying neural mechanisms.

There are several novel aspects of our investigations. First, we employ a stochastic whole-brain model to simulate large-scale neural dynamics[34] using as input the directly measured structural connectivity of a stroke patient or healthy control. Importantly, we do not fit the resulting dynamics with empirical measured functional connectivity. The structural connectivity, measured at two time-points: 3 months after stroke (t_1) and one year after stroke (t_2), or three months apart in healthy controls, was used to build personalized whole-brain models. This method allows measuring departures from normal criticality at the group level or in individual subjects, as well as the recovery of criticality over time. This approach contrasts with other studies that used average or atlas-based structural connectivity models to simulate activity time courses[35–43]. For example, a recent study by Haimovici et al. found that lesions push the system out of criticality towards a sub-critical state[44]. However, these theoretical results were not validated with real patient data. Other studies found abnormal global metrics of network function, such as information capacity, integration, and entropy in stroke patients as compared to healthy subjects[45,46]. However, these models were not personalized, i.e., did not use directly measured individual structural connectivity but healthy group average structural connectomes that were fit with many (hundreds) free model parameters to minimize the distance between the model and the empirical functional connectivity[45].

Secondly, we apply this computation model strategy to a unique cohort of stroke patients studied prospectively and longitudinally at Washington University in St. Louis. This cohort has been investigated with a large battery of neurobehavioral tests, as well as structural, structural and functional connectivity magnetic resonance imaging at three months and 12 months post-stroke. This cohort is representative of the stroke population both in terms of behavioral deficits, their recovery, and the lesion load location[47]. In previous work, we have characterized the behavioral, structural, and functional connectivity abnormalities in this cohort and their relationship to behavioral impairment and recovery[32,33,48–50] (see Corbetta et al.[51] for a review). In network terminology, strokes cause an acute decrease of modularity that normalizes over time[32,52]. Here we relate alterations of criticality to behavioral deficits, and compare criticality computed on the model with empirical measures of functional connectivity.

The paper is organized as follows. In the Result section, we first describe our stochastic model embedded in the large-scale structural brain network. Then we describe the behavior of the system for different values of the (unique) control parameter. We first compare the dynamical patterns between controls and patients; then, we show a remarkable recovery pattern across time-points. We then investigate the corresponding functional connectivity and behavioral correlations. Finally, we relate the individual variability in criticality, as well as changes of criticality overtime to specific anatomical (sub-)networks using machine learning techniques.

Results

Simulation of large-scale neural dynamics

To simulate neural activity at the individual whole-brain level we employed the homeostatic plasticity model recently developed in[34]. Figure 1 illustrates the main ingredients of our modeling strategy. Individual structural connectivity matrices are the key input of the stochastic model (Fig. 1A). Imaging and behavioral data are taken from a large-scale stroke study described in previous publications[33,47,53]. Structural connectivity data was available for 77 patients, acquired three months (t_1) and one year (t_2) after stroke onset. The same study includes data from 28 healthy controls, acquired twice at a distance of three months (see Methods sections for details about the stroke dataset, lesion analysis, diffusion weighted imaging (DWI), and resting-state functional MRI (R-fMRI)).

The system is described as a network of $N = 324$ nodes (i.e., cortical brain regions), linked with symmetric and weighted connections obtained from DWI scans and reconstructed with spherical deconvolution[54,55]. The weights of the structural connectivity matrix, W_{ij}, describes the connection density, i.e, the number of white matter fiber tracts connecting a given pair of regions of interest (ROIs) normalized by the product of their average surface and average fiber length[56]. The ROIs are derived from a functional atlas of the cerebral cortex[57]. Fig 1A shows the topography of structural connections, the corresponding network assignment, and the corresponding structural matrix. The matrix is sparse, and contains predominantly short-range connections. In the control group, inter-hemispheric connections between homotopic regions of the same network are visible (dorsal view of the brain Fig. 1A). In the stroke patients, inter-hemispheric connectivity is decreased, as shown by Griffis et al.[33] who found that loss of inter-hemispheric connectivity - both structural and functional - is the predominant aberrant pattern in stroke. The lesion load topography in the stroke cohort is shown in Supplementary Material (Fig. S1) and matches the topography of larger cohorts[47]. When the lesion damages a cortical ROI, even partially, those nodes were removed from the simulation. Therefore, only structurally normal regions were considered in the analysis. The same procedure was adopted for

bioRxiv preprint doi: https://doi.org/10.1101/2020.12.17.423349; this version posted December 20, 2020. The copyright holder for this preprint (which was not certified by peer review) is the author/funder, who has granted bioRxiv a license to display the preprint in perpetuity. It is made available under aCC-BY-NC-ND 4.0 International license.

controls, but in this case the presence of isolated nodes is rare, due to reconstruction errors/fluctuations of the brain networks topologies.

Cortical activity is modeled through stochastic dynamics based on a discrete cellular automaton with three states, namely, active (A), inactive (I), and refractory (R). The state variable of a given node i, $s_i(t)$, is set to 1 if the node is active and 0 otherwise. The temporal dynamics of the i-th node is governed by the transition probabilities between pair of states: (i) $I \to A$ either with a fixed small probability $r_1 \propto N^{-1}$ or with probability 1 if the sum of the connections weights of the active neighbors j, $\sum_j W_{ij}$, is greater than a given threshold T , i.e., $\sum_j W_{ij} s_j > T$, otherwise $I \to I$, (ii) $A \to R$ with probability 1, and (iii) $R \to I$ with a fixed probability r_2[34]. The state of each node is overwritten only after the whole network is updated. Therefore, during the temporal dynamics, a node activation happens (most frequently) when the incoming input excitation from its nearest active neighbors exceeds a fixed threshold T , i.e, $\sum_j W_{ij} s_j > T$. In other words T plays the role of a threshold parameter that regulates the propagation of incoming excitatory activity. On the other hand two parameters r_1 and r_2 controls the time scale of self-activation and recovery of the excited state[34,58]. As we clarify in the methods section, r_1 and r_2 are set as a function of the network size, while T is the control parameter of the model.

Following[34,59], we consider homeostatic plasticity principles regulating network excitability by introducing a normalization of the structural connectivity matrix

$$\widetilde{W}_{ij} = W_{ij} / \sum_j W_{ij}. \tag{1}$$

As shown by[34], the above normalization facilitates the emergence of functional networks at rest, and increases the correlation coefficients between model and empirical data. More importantly, it minimizes the variability of the neural activity patterns and the critical point of the stochastic model for different subjects, allowing the opportunity of statistical comparison among model outputs for single individuals.

For each individual (time-point) we calculate the following neural state variables (see Methods section): the average activity (A), the standard deviation of the activity (σ_A), and the size of the averaged clusters, the largest (S_1), and the second largest (S_2), as a function of the activation threshold T. These clusters of activity are defined as the size of the connected components of the graph defined by the sets of nodes that are both structurally connected to each other and simultaneously active[34]. In the numerical experiments, we set the total simulation time-steps $t_s = 1000$, in order to recover the length of typical fMRI experimental time-series ($\sim$ 15 min).

A typical behavior of the simulated brain activity for different values of T , while keeping r_1 and r_2 fixed, is illustrated in Fig. 1C. The brain dynamics displays a phase like transition at critical threshold T_c given by the corresponding value of T. In fact, at $T = T_c$ brain activity has the largest variability, the maximal second largest cluster size, and a steep change in the first cluster size[34,60,61]. In contrast, for small values of the activation threshold ($T \ll T_c$), the system is characterized by high levels of excitation, i.e, the signal from an active node will easily spread to its neighbors. In this scenario, we have the so-called super-critical or disordered phase, which is characterized by sustained spontaneous activity with fast and temporally uncorrelated fluctuations (Fig. 1D, blue time-series). On the other hand, high values of T ($T \gg T_c$) lead to a sub-critical or ordered phase, which is characterized by regular, short propagating and not self-sustained activity. In this case, only those nodes with the strongest connections will determine the excitation flow in the network. In the sub-critical phase, simulated BOLD signals have very small correlations (Fig. 1D, green time-series). The critical phase appears in between of these two states, when brain activity displays oscillatory behavior and long-range temporal correlations of their envelope[34,44,60]. In this phase, the simulated BOLD activity shows the highest correlation (Fig. 1D, red time-series)[34].

In the next sections, first, we present simulations of the whole brain model with homeostatic plasticity for stroke and control individuals, as well as at the group level. Next, we study the structural connectivity correlates of neural dynamics alterations induced by stroke lesions. Third, we identify components of the structural networks that are most strongly related to criticality and its recovery over time. Fourth, we compare the simulations output with empirical functional networks, and with behavioral data obtained in multiple domains (e.g., language, motor, memory) from an extensive neuropsychological battery (see Methods section).

Abnormal neural dynamics in stroke

Figure 2(A-D) shows the model's neural activity variables for an arbitrary control-patient pair. Results are similar for other individuals, see Supplementary Material (Figs. S2 to S8). To facilitate the comparison among individual neural patterns of healthy individuals and stroke patients, we also present the average and standard deviation of the healthy controls (blue dashed line and shaded area, respectively). In general, neural dynamics in healthy participants are quite distinct from those of a typical stroke patient. First, let us consider one healthy participant, Fig. 2(A-B) (black/gray dots). The neural patterns follow the expected behavior, with a critical point $T = T_c$ around the maximum of S_2, or equivalently, near the sharp decrease of S_1. Moreover, as expected, the two curves have low variability across the two scanning time-points (t_1 and t_2), displaying the same T_c (within one standard deviation), and stable shape as a function of T.

bioRxiv preprint doi: https://doi.org/10.1101/2020.12.17.423349; this version posted December 20, 2020. The copyright holder for this preprint (which was not certified by peer review) is the author/funder, who has granted bioRxiv a license to display the preprint in perpetuity. It is made available under aCC-BY-NC-ND 4.0 International license.

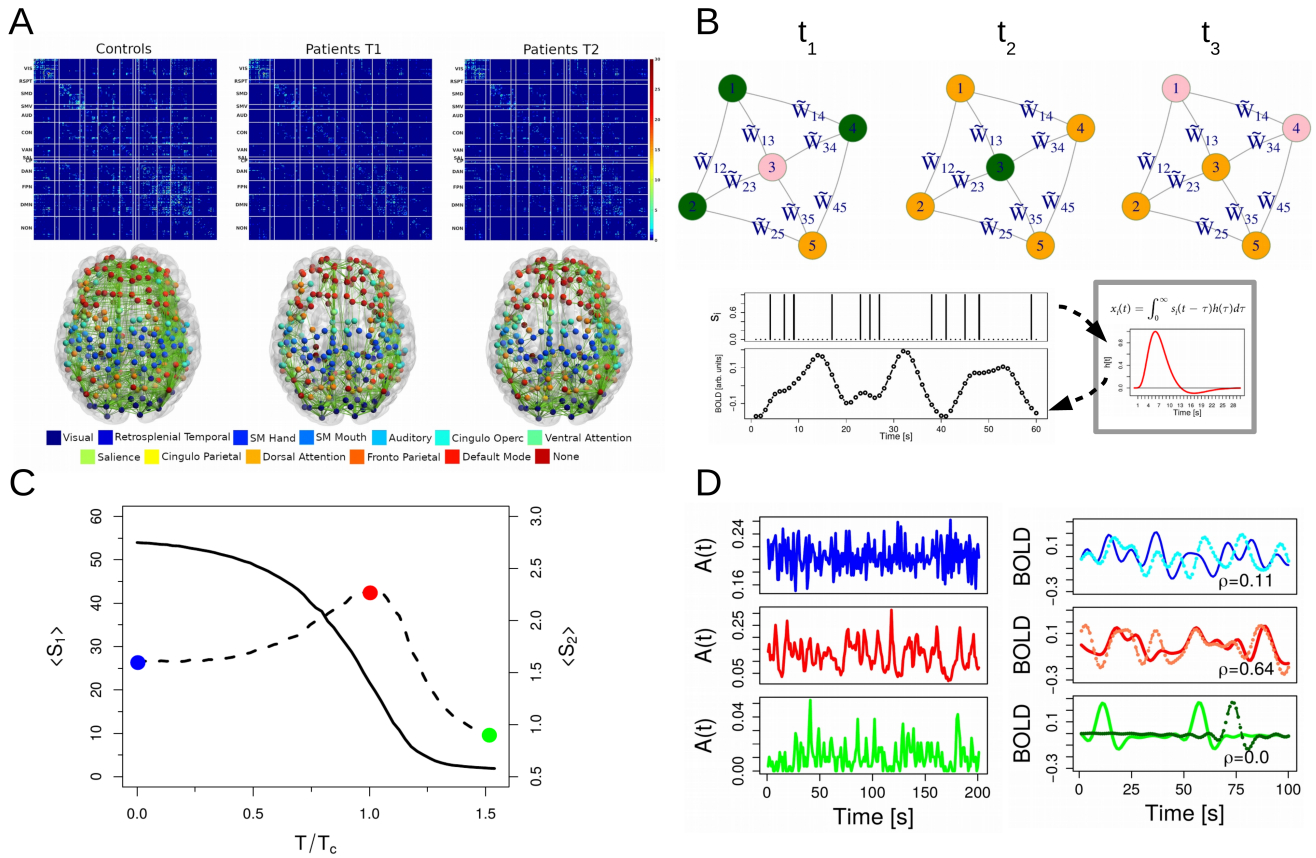

Figure 1. A) Average structural connectivity (SC) matrices (top) and their corresponding network architecture embedded in a glass dorsal view of the brain (bottom). SC matrices and brain networks are organized according to regions of interest (ROI) defined on the cortical parcellation of Gordon et al.[57]. B) Top. Illustration of the network dynamics with homeostatic plasticity following the transition probabilities between the three possible states: inactive (I), active (A) and refractory (R). The temporal evolution of the central inactive node (pink) is as follows: in t_1, it is surrounded by three active nodes (green) and one refractory node (orange); in t_2, the incoming excitation is propagated ($\widetilde{W}_{31}+\widetilde{W}_{32}+\widetilde{W}_{34}>T$); and finally, in t_3, it reaches the refractory state. Bottom. Procedure used to transform node's activity, $s_i(t)$, in functional BOLD signals, $x_i(t)$. BOLD time-series are obtained by convolving instantaneous $s_i(t)$ with a canonical hemodynamic response function (HRF). C) Behavior of the neural variables, the largest (S_1 , continuous line), and the second largest (S_2 , dotted line) cluster size as a function of T. The peak in S_2 (red dot) is identified as the (percolationlike) phase transition[61]. Blue and green dots correspond to minimal and maximal values of T, and corresponding activity and BOLD time-series in panel D. D) Left panel: instantaneous network activity, $A(t)=\sum_i s_i(t)/N$, for different values of the activation threshold T; the super-critical phase $T \ll T_c$ (blue time-series), the critical phase $T=T_c$ (red) and the sub-critical phase $T \gg T_c$ (green). Right panel: example of the simulated BOLD signals between two arbitrary ROIs and their corresponding Pearson correlation ρ. The highest correlation is achieved at the critical phase, where BOLD fluctuations are long-range correlated.

bioRxiv preprint doi: https://doi.org/10.1101/2020.12.17.423349; this version posted December 20, 2020. The copyright holder for this preprint (which was not certified by peer review) is the author/funder, who has granted bioRxiv a license to display the preprint in perpetuity. It is made available under aCC-BY-NC-ND 4.0 International license.

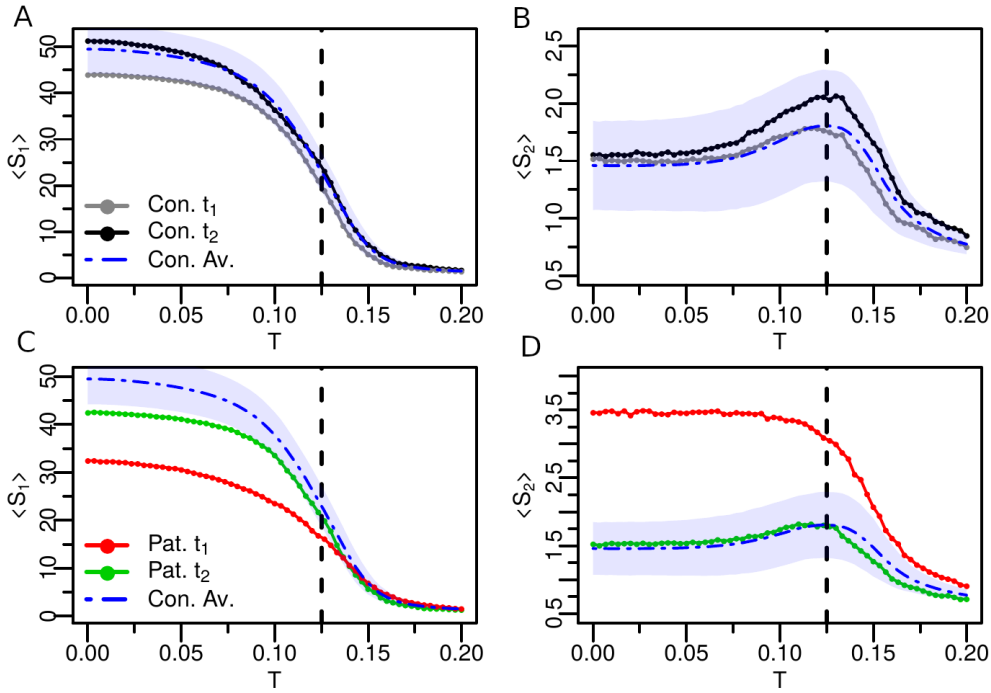

Figure 2. Individual based analysis of neural activity patterns, S_1 and S_2, of a healthy participant (Con. / A-B) and stroke patient (Pat. / C-D). In blue dashed line we show the corresponding control's group average; while the shaded area corresponds to one standard deviation. For the control, t_1 and t_2 correspond at two different time points 3 months apart. For the patient, t_1 and t_2 correspond to 3 month and 12 month time points post-stroke. The healthy participant exhibits conserved shape across time points, with small variability across time points. For the stroke patient under consideration, the flattened shape at t_1 of both, (S_1) and (S_2), indicates a decreased strength of the critical phase transition, which, however, improves at t_2.

The pattern is dramatically different in the stroke subject. The strength of the critical transition, as described by the characteristic peak in S_2[34] (or equivalently, the sharp decrease around T_c in S_1), is much flatter at three months post-stroke, but seems to normalize at one year, where the transition is sharper and both, S_1 and S_2, behave similarly to the control case. As already observed in[34], the homeostatic normalization on the weights of the structural matrix decreases the inter-subject variability of neural activity patterns. More importantly, it fixes the critical point of all individuals to a universal value, $T_c \sim 0.125$. In other words, thanks to the homeostatic plasticity mechanism, the critical point is independent of the individual variability in the structural connectivity matrix. However, the strength of the S_1 and S_2 peaks provides an individual characterization of differences in criticality. In fact, at the vicinity of the critical point the differences in the stroke patient at t_1 and t_2 are pronounced. The most interesting feature, as shown in Figs. 2(C-D), is the recovery-like pattern: the one-year post-stroke curve resembles, both qualitatively and quantitatively, the pattern of the healthy subject. Similar results are shown for several examples of individual stroke patients and healthy subjects in the Supplementary Material (Figs. S2 to S8). Euclidean distance, $d(t_1,t_2)$, is then used to quantify the similarity between pair of curves corresponding to a given neural activity pattern (e.g. S_2) at the two different time points (see Methods section, (9)). A low $d(t_1,t_2)$ indicates low variability across time points either of normal or abnormal dynamics. High $d(t_1,t_2)$ indicates changes of the neural state variables across times. Figure 3 (A-B) shows the normalized distribution of the Euclidean distances for all individuals in the data set for S_1 and S_2, respectively. Confirming our observations, there is much greater variability in stroke patients than in control subjects. The dispersion of the distribution $p(d)$ measured for the healthy participants provides a benchmark for estimating the intrinsic inter-individual variability of individual brain criticality. On the other hand, the large spread of $p(d)$ in the stroke population indicates that differences in criticality between 3 months and one year need to be accounted for by changes in the structural connectivity. In other words, variability in the patient's criticality should be related to differences in the underlying structural anatomy. This interesting biological insight will be examined in more detail in the next section.

We next examined whether these dynamical features were robust at the group level. Figure 3(C-D) summarizes our main results for S_1 and S_2 (see Supplementary Material, Fig. S9, for the other variables). The thin solid curves represent each single individual, while the heavy solid ones represent the group average, i.e., $X^{av} \equiv \sum_i^n X(i)/n$, where n is the number of individuals in each group. The first result is the almost perfect collapse of S_2 over the entire range of T between controls and patients at

bioRxiv preprint doi: https://doi.org/10.1101/2020.12.17.423349; this version posted December 20, 2020. The copyright holder for this preprint (which was not certified by peer review) is the author/funder, who has granted bioRxiv a license to display the preprint in perpetuity. It is made available under aCC-BY-NC-ND 4.0 International license.

one year post-stroke (a perfect collapse is also observed for σ_A, see Supplementary Material Fig. S9). Even in the vicinity of the critical point, where the greatest variability is expected, the two curves are very close and statistically equivalent within one standard deviation. We interpret this dynamical feature as a return of the stroke group at 12 months toward normal criticality levels. Following the same line of reasoning, we interpret the broader peak of S_2 at 3 months as a deviation from the healthy baseline levels of criticality. In t_1, activity clusters are more segregated, as expressed by large S_2 (or correspondingly, small S_1, i.e., the first component is broken down into larger second clusters). In t_2, this abnormal condition is restored, and S_2 decreases toward normal, while S_1 increases. These changes in cluster sizes reflect alterations in segregation-integration balance within/between networks[62]

In summary, both in single subjects and group level, the models of stroke patients show a significant loss of the normal critical dynamics at three months that recovers at one year for most patients. This is consistent with the first hypothesis that criticality is a property of the normal brain structural architecture. Next, we examine the anatomical bases of brain criticality modifications.

Structural connectivity related to criticality and its recovery

The recovery of criticality from three to twelve months, as unveiled from our modeling studies, must reflect a change in the underlying structural connectivity. To investigate which connections are more strongly related to the alteration and recovery of criticality, we used a multivariate machine learning approach, based on cross-validated Ridge Regression[63], to relate the model's neural activity variables to the structural connectivity matrix. This approach allows to identify edges (and sub-networks) across the whole brain that are most strongly related to the variable of interest (see Methods for details).

First, we investigate the relationship between structural connectivity and criticality, both in controls (using the t_2 matrix) and in one-year post-stroke patients. Figure 4 shows that the structural connectivity accounts for a large proportion of variance in S_1 (controls: $R^2 = 0.50$; patients: $R^2 = 0.48$). Interestingly, the map of predictive edges in controls shows that inter-hemispheric connections are related to higher criticality values (i.e, positive edges). Indeed, for the 200 most predictive edges shown in Fig. 4, 9% are inter-hemispheric, 91% intra-hemispheric, summing up to 81% positive edges. In contrast, predictive maps of patients show a different organization, with most inter-hemispheric edges pointing to the visual network, and a small decrease in the overall number of inter-hemispheric connections, 7% out of 200 edges. In the Supplementary Material, Fig. S10, we show a similar connectivity pattern for the second cluster (S_2) (controls: $R^2 = 0.35$; patients: $R^2 = 0.46$).

Next, we computed recovery of criticality as the difference of S_1 (evaluated at the critical point) between the two time points, i.e., $S_1(t_2 - t_1)$. Large values would index a normalization of criticality toward the control baseline (as illustrated in Fig. 3C). We used the structural connectivity matrix at t_1 as a predictor of $S_1(t_2 - t_1)$. In this way, we were able to quantify the role of the structural damage in constraining or facilitating the patient's recovery. The results, reported in Fig. 5, show that criticality (and its recovery) is related to structural links involving the default mode network and the networks subserving attention and executive control (cingulo-opercular network, dorsal attention network).

Finally, to investigate whether the structural connections predictive of the recovery of criticality were part of the normal functional architecture, and did not reflect random connections, we correlated the number of predictive edges for each node (ROI) with the corresponding node's strength in the healthy controls' average functional connectivity. The high correlation ($\rho = 0.98$ for positive/negative edges vs. node functional connectivity) indicates that the predictive edges are not random, but consistent with the normal variability of the brain functional architecture.

Relationship between recovery of criticality, functional connectivity, and behavior

Up to this point, our results strongly suggest that post-stroke rehabilitation induces a normalization of the neural activity patterns that can be quantified by criticality. One important question is whether these dynamical signatures reflect the patients' recovery as typically seen in behavioral measures[53] and in the functional connectivity[32]. We used the framework described in[34] to simulate the functional connectivity from the structural one for each individual patient. Briefly, the time-series of node's activity, $s_i(t)$, is convolved with a canonical hemodynamic response function (HRF). We further applied a band-pass filter in the range of $0.01 - 0.1$ Hz. Next, we obtain the functional connectivity matrix, FC, through the Pearson correlation, (6), between each pair of ROIs in the network[44]. We use the averaged correlation across ROIs FC to characterize the strength of the functional connections in patients and controls (see (7)). We also compute the entropy, H, of the functional matrices following the framework of Saenger et. al.[46] (see Methods section, (8)). The entropy measures the repertoire diversity and the complexity of the functional connections, and may serve as a biomarker of stroke recovery as well[46]. The behavioral performance of patients and controls was inferred from a neuropsychological battery measuring performance in 8 behavioral domains (motor, visual, language, verbal and spatial memory, attention visual field, attention average performance, attention shifting)[47]. Here we use the average factor score obtained from averaging normalized factor scores for each domain[47], $\langle B \rangle = \sum_i B_i/8$, to characterize the individual's overall performance.

In order to quantity the relationship between dynamical, functional connectivity and behavioral features we shall use the critical point as a biomarker. Indeed, for each simulated quantity ($\langle X \rangle$) (averaged over 50 samples with initial random

bioRxiv preprint doi: https://doi.org/10.1101/2020.12.17.423349; this version posted December 20, 2020. The copyright holder for this preprint (which was not certified by peer review) is the author/funder, who has granted bioRxiv a license to display the preprint in perpetuity. It is made available under aCC-BY-NC-ND 4.0 International license.

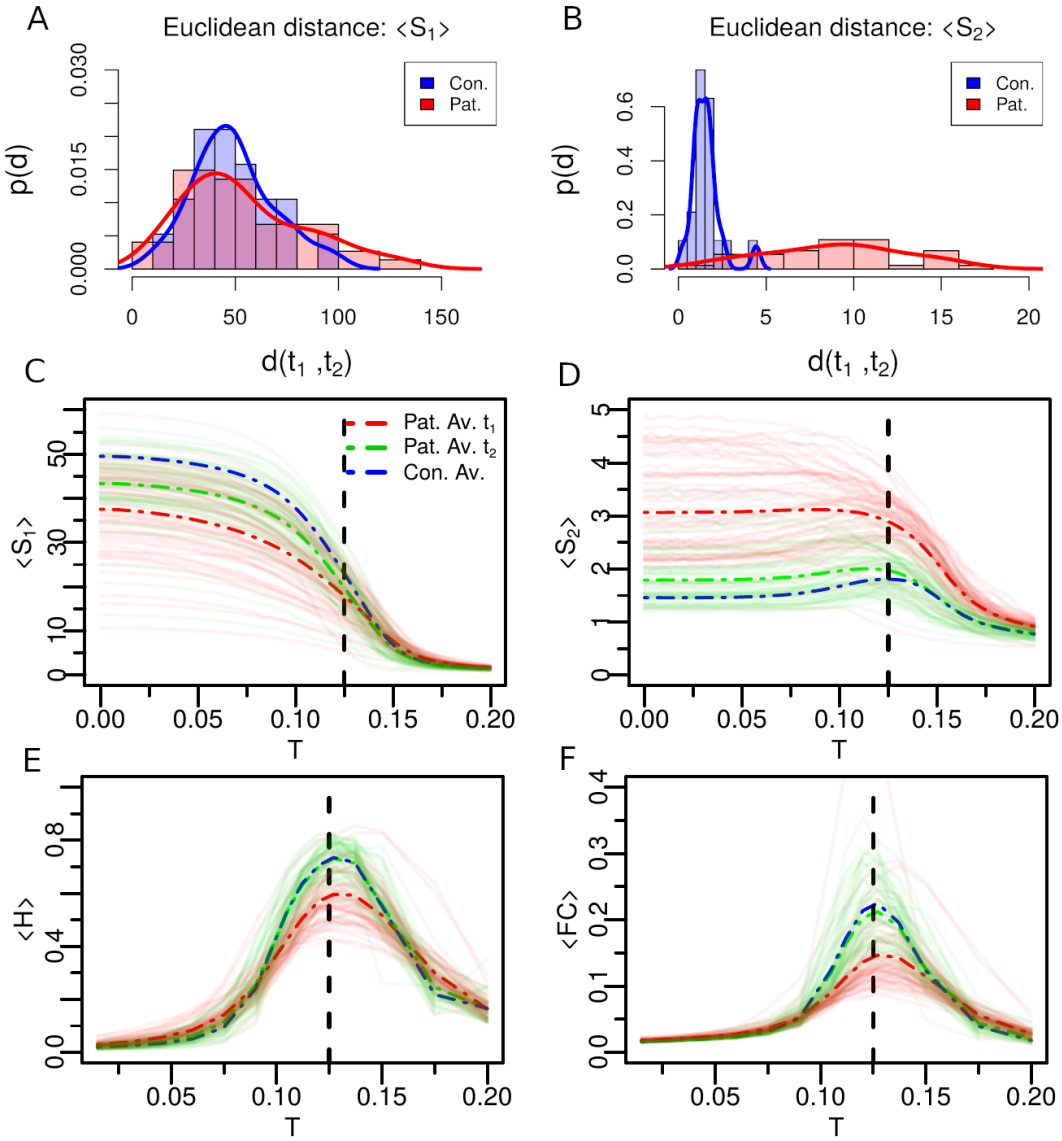

Figure 3. A) The Euclidean distance, $d(t_1,t_2)$ of S_1 values across time points in individual age-matched-controls (Con.) and stroke patients (Pat.). B) The same for S_2. Patients show greater variability in model neural activity. C-D) Group based analysis of neural activity patterns, S_1 and S_2, as a function of T for all patients and controls. Red lines represent patients at t_1 (3 months post-stroke), while green lines at t_2 (12 months post-stroke). The thin solid curves represent each individual stroke patient, while the heavy dotted lines represent the group average. The group analysis reveals that levels of criticality approach normal levels at t_2 while they are significantly abnormal at t_1. Thanks to the homeostatic normalization, the critical points are practically the same for all individuals (black vertical dashed line). E-F) Model entropy H (see Methods section, (8)) and the average functional connectivty FC averaged across ROIs (see Methods section, (7)) for patients and controls individuals, as a function of T. Note improvement of H and FC over time and trend toward normalization of these simulated functional measures.

bioRxiv preprint doi: https://doi.org/10.1101/2020.12.17.423349; this version posted December 20, 2020. The copyright holder for this preprint (which was not certified by peer review) is the author/funder, who has granted bioRxiv a license to display the preprint in perpetuity. It is made available under aCC-BY-NC-ND 4.0 International license.

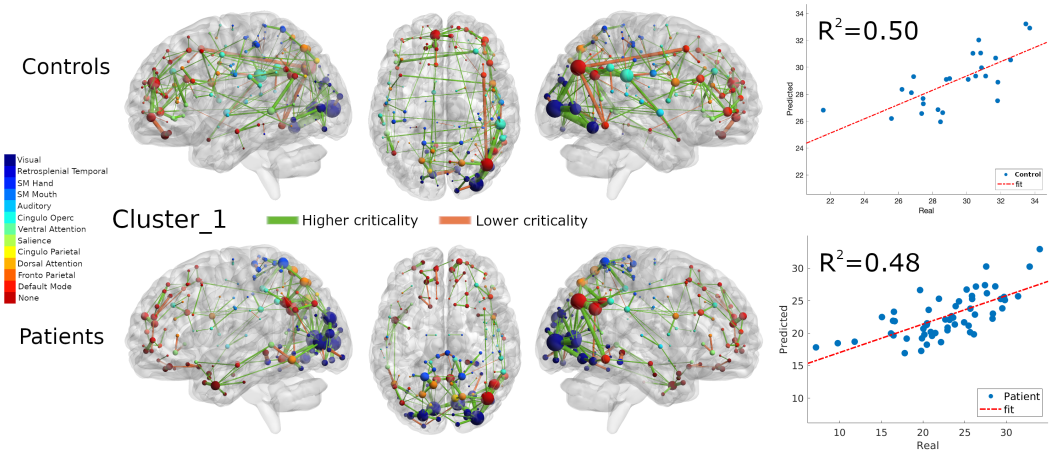

Figure 4. Structural connectivity related to criticality (first cluster size S_1). Structural edges at t_2 that predict higher (green edges) and lower criticality (orange edges) values at t_2 (top: Controls; bottom: Patients). The size of each ROI, colored by network, corresponds to the number of predictive edges converging on it. The scatter plot shows real vs. predicted criticality values from the Ridge Regression model.

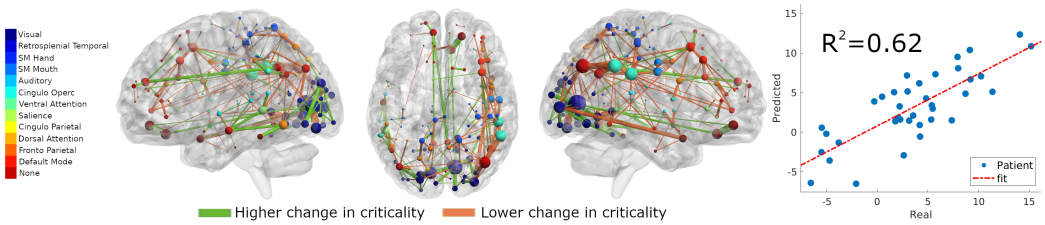

Figure 5. **Top**: Structural connectivity related to the recovery of criticality (first cluster size S_1). Structural edges at t_1 that predict higher and lower criticality changes in S_1 from t_1 to t_2.

bioRxiv preprint doi: https://doi.org/10.1101/2020.12.17.423349; this version posted December 20, 2020. The copyright holder for this preprint (which was not certified by peer review) is the author/funder, who has granted bioRxiv a license to display the preprint in perpetuity. It is made available under aCC-BY-NC-ND 4.0 International license.

configurations), we define the recovery index as $X(t_2 - t_1) = \langle X \rangle_{t_2} - \langle X \rangle_{t_1}$, where both time points are computed at the critical point. We choose the critical point because at this state we have the best matching between empirical and model data, although no fitting is performed[34]. For the empirical data, the recovery index is obtained in the same way, as a difference between the averages of two given behavioral/functional features at time t_1 and t_2. In what follows, the subscript "m" stands for model, while "e" stands for empirical.

In Supplementary Material, Figs. S3 and S4, we show the simulated H and FC, for the same pair of individuals considered in Fig. 2 (ID AMC: 19, ID PAT: 12), as a function of T. Far from the critical dynamics, i.e., $T \gg T_c$ and $T \ll T_c$, both variables are vanishingly small, while a maximum happens very close to the critical state ($T = T_c$). We find that the values of both H and FC from t_1 to t_2 evolve towards the control's baseline, suggesting a functional recovery of the analyzed patients.

The group analyses are illustrated in Fig. 3 (E-F). Normalization of H and FC across time-points is very robust, and patients at t_2 are likely to display functional attributes (i.e., mean values) similar to controls. Interestingly, a recovery of the dynamical activity patterns, (S_1) and (S_2), leads to an increase in functional complexity, (H), and in the average correlation, (FC), being consistent with a return of critical dynamics.

We find a significant correlation ($R^2 = 0.8$ and $\rho = 0.9$) on the time dependence of the averaged behavioral factors, computed at t_1 and t_2 (Fig. 6A). This result reveals that B is indeed a robust feature of individuals across time, otherwise we would have found a scrambled scatter plot with negligible correlation. Notably, $S_2(t_2 - t_1)$ was correlated with $B(t_2 - t_1)$ ($R^2 = 0.31$ and $\rho = 0.58$; Fig. 6B), but not separately at each time-point (see Supplementary Material, Fig. S11 A-B). This result shows that it is the change in the dynamic state of the brain (S_2) from t_1 to t_2 that is sensitive to behavioral changes. The correlation is negative as a large difference in S_2 value - with bigger S_2 clusters at 3 months vs. 12 months - correlates with a strong change in behavioral scores. These findings are consistent with the second prediction that variations in neural dynamics are behaviorally relevant.

Next, we considered the relationship between neural dynamics and functional connectivity, a well studied biomarker of stroke / behavior relationships[32,33]. As a whole brain marker of functional connectivity, we employed the average FC across all ROIs. We found that variations in neural variability, as described by $S_2(t_2 - t_1)$, was significantly correlated with the model average functional connectivity FC_m ($R^2 = 0.45$ and $\rho = 0.68$; Fig. 6C). The correlation was negative: large decreases of S_2 over time, i.e. smaller S_2 clusters hence more segregated networks, correlated with large longitudinal changes in average functional connectivity (Fig. 6C). The negative relationship between S_2 and FC_m was present both at t_1 and t_2 (Supplementary Material, Fig. S11 C-D), which is consistent with a robust relationship between dynamic measures and functional connectivity.

In addition, since studies on stroke have highlighted the specific behavioral importance of homotopic functional connectivity, i.e. inter-hemispheric connections between symmetrical regions belonging to the same network[50,64,65], we examined the relationship of average FC vs. homotopic FC, both empirical - measured directly - and model, with behavioral performance. Empirical $FC_e(t_2 - t_1)$ correlated with homo-$FC_e(t_2 - t_1)$ ($R^2 = 0.58$, $\rho = 0.77$ and p-value < 0.05); in addition, both measures predicted a significant amount of behavioral variability $B(t_2 - t_1)$ (p-value < 0.05), with homo-FC$_e$ providing slightly higher prediction than the average FC_e (see Fig. 6 D-F). We repeated the same analysis, but for the model generated data (Fig. 6 G-I). The stochastic whole-brain model poised at the critical point was capable of reproducing all behaviors observed empirically (Fig. 6 D-F). Interestingly, it predicted more variability than the empirical data for the relationship among $FC(t_2 - t_1)$ and homo-$FC(t_2 - t_1)$ with $B(t_2 - t_1)$. As the critical signatures restore over time, patients exhibit increased functional and behavioral performance. Similar results were obtained for entropy (Supplementary Material Fig. S12).

On the other side, we did not find any relationship between S_2 and FC_m with FC_e (results not shown). This is expected since we have not optimize the model inputs to reproduce the empirical FC; in other words, we do not employ a fitting procedure to generate the model FC data as done for example in[45].

Discussion

We set out to examine whether criticality is affected by lesions, and whether alterations of criticality are behaviorally relevant. We use lesions as a causal manipulation to test the theory that criticality is a fundamental property of healthy brains that provides optimal functional and behavioral capabilities. Several interesting results are worth of discussion.

First, our stochastic model is personalized since it used as input direct estimates of structural connectivity at the individual level. The model provides measures of activity, functional connectivity, and criticality that tracked individual variability in healthy and stroke participants. Importantly, alterations in stroke patients were evident both at the group and individual level, and easily separated stroke from healthy subjects. Second, these criticality alterations normalized over time. This normalization reflect changes of the underlying structural connectivity. We describe which connections are most predictive of the final level of criticality, and which predict improvements in criticality. The distribution of predictive connections was not random but matched the normal functional architecture of the healthy brain. Third, we show that alterations of criticality were behaviorally relevant as they correlate with improvements in performance. Alterations of criticality correlated with variations of activity, entropy, and performance improvements, that are also captured in the model.

bioRxiv preprint doi: https://doi.org/10.1101/2020.12.17.423349; this version posted December 20, 2020. The copyright holder for this preprint (which was not certified by peer review) is the author/funder, who has granted bioRxiv a license to display the preprint in perpetuity. It is made available under aCC-BY-NC-ND 4.0 International license.

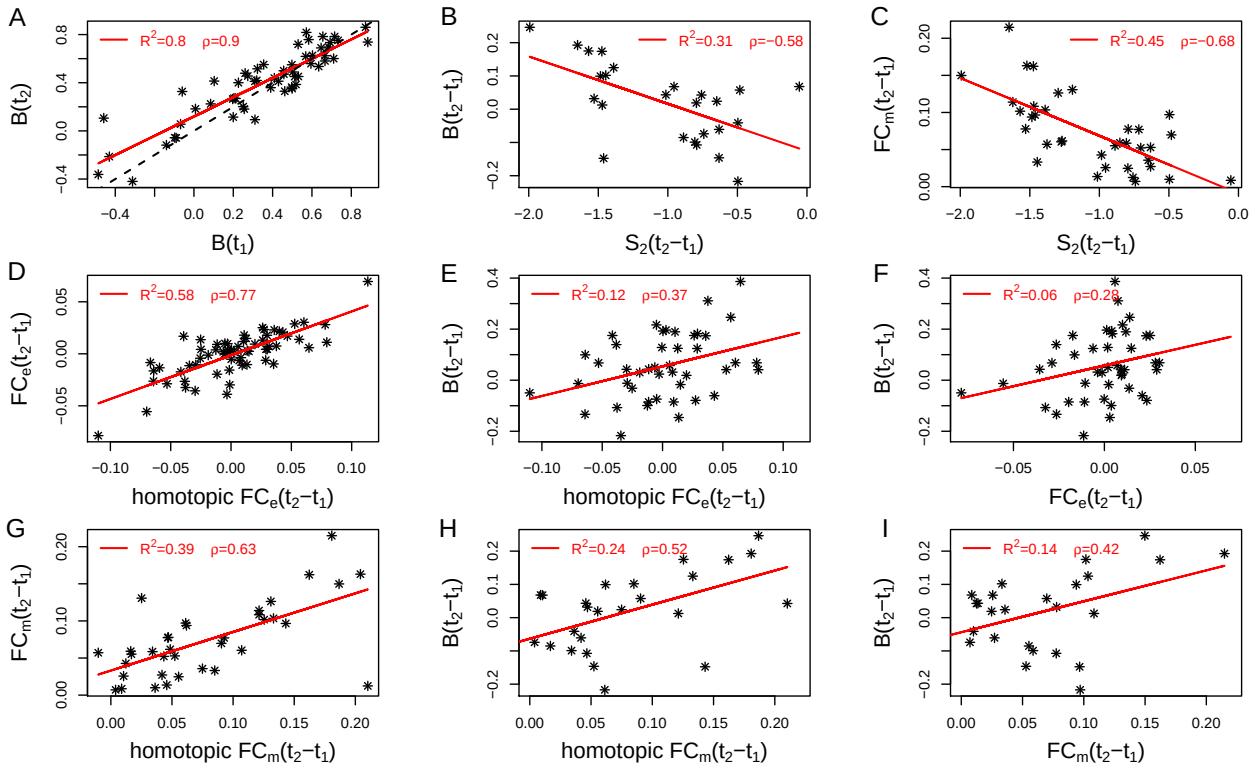

Figure 6. Statistical correlates between dynamical, functional and behavioral patterns at criticality. In the legend we show the (linear) correlation, ρ and the R^2. All linear regressions have p-value < 0.05. Agreement between empirical and model data is clear.

bioRxiv preprint doi: https://doi.org/10.1101/2020.12.17.423349; this version posted December 20, 2020. The copyright holder for this preprint (which was not certified by peer review) is the author/funder, who has granted bioRxiv a license to display the preprint in perpetuity. It is made available under aCC-BY-NC-ND 4.0 International license.

Methodological considerations

The whole-brain mesoscopic model, a variant of the Greenberg-Hastings cellular automata[66], was proposed by Haimovici et al.[58]. When poised at the critical point, the model is able to capture, at the group level, the emergence of experimental spatiotemporal patterns, the temporal correlation between regions (functional connectivity, FC), the organization of brain wide patterns in so called resting state networks (RSNs), and the scaling law of the correlation length, among others.

We improved the Haimovici model by adding a normalization to each node's excitatory input, a mechanism of homeostatic plasticity[67–69]. This simple adjustment balanced the macroscopic dynamics increasing the strength of critical transitions. The clusters of activity became more heterogeneous spreading along the whole network and not mainly in the hubs, as in the not-normalized model. In the normalized model, the cluster size distribution in proximity to the critical point follows a truncated power-law with a critical exponent α close to the hallmark exponent of avalanches sizes, $\alpha = 3/2$. In contrast scaling invariance in the cluster size distribution is not visible in the absence of normalization. Finally, the homeostatic normalization mechanism significantly improves the correspondence between simulated and empirical functional networks based on fMRI.

An important feature of the normalized model is that it minimizes the variability of the critical points and neuronal activity patterns among healthy subjects. The normalization collapses the model state variables of healthy subjects into universal curves, which allows to compare critical points between patients and stroke, and stroke patients at different time points.

Another important innovation is that the input to the model were individually measured structural connectomes, both healthy and stroke individuals at two time points. The repeated measures allowed the estimation of the stability of the criticality values, which were quite narrow in healthy subjects, thus supporting that changes of criticality were related to the effect of the lesions.

The availability of individual structural connectomes is not common, and most whole-brain studies have used population atlases of white matter connections[45,70]. Also, fMRI connectivity is often used to enhance the accuracy of structural connectivity due to its low sensitivity or incomplete coverage[45,46]. Our structural connectivity data were sparse, with a negative exponential small world distribution, and weaker inter-hemispheric connections in stroke patients consistently with recent work[48,49]. However, the model can be certainly improved. The DWI data were not state-of-the-art. The sequence was 10-year old with 60 directions and a single b-value of 1000 s/mm^2. This group of healthy and stroke subjects began enrollment in a prospective stroke study at Washington University in 2010 with completion in 2015. In future work, we will have access to subjects studied with multi-shell, multi-directional and multi-weighted diffusion weighted images. Another limitation is that data is available only at 3 months and 12 months for fear that diffusion imaging at 2 weeks, the first time point in the study, was too noisy. In the new cohort we will have access to 2-week data. This is important as most recovery occurs between 2 weeks and 3 months.

We simulated fMRI functional connectivity by augmenting the stochastic whole brain personalised model with a standard hemodynamic pipeline. We used the average (across ROIs) and inter-hemispheric homotopic functional connectivity (FC) and entropy (H, which measures the functional weight diversity) to characterize stroke-related changes. The model reproduced changes of functional connectivity observed empirically in stroke, such as a decrease of inter-hemispheric FC[33,49,50,64,65] and entropy[46], subsequent normalization[32], and correlation with behavioral performance[33]. However, the model's fit with empirically measured FC was low (results not shown). We elected not to optimize the input through functional connectivity because it would have hidden the role of structural connectivity in supporting a critical phase transition in stroke patients and its progression following treatment. Fitting the model with free parameters has its own issues including sloppy parameter sensitivities[71], identifiability problem[72] and overfitting issues[73]. More importantly, this work aims at unveiling robust and universal features of brain criticality in relation to the anatomical brain connectivity structure and focal lesions, and therefore it is crucial that the model dynamics has the smallest possible degrees of freedom[74].

Stroke lesions cause changes in activity, entropy, and criticality

Whole-brain models of healthy controls showed stable patterns of neural activity, both across time-points and individuals. It is important to understand the model dynamics in healthy subjects before considering changes in stroke. For low thresholds of activation, the system is super-critical with high levels of activity, low entropy, low levels of functional connectivity, and a single giant first cluster (S_1) (Fig. 3, Suppl. Material, Figs S2-S8). This is akin to a brain in status epilepticus with very high level of activity but low entropy, hence no efficient processing of information and lack of consciousness. For very high thresholds of activation, the system is sub-critical with low levels of activity, low functional connectivity, and entropy. Activity is mostly local with small clusters (S_1). For intermediate thresholds, the neural patterns followed the expected behavior, with a phase transition peaking around the maximum of S_2 (Fig. 3, Suppl. Material, Figs. S2-S8). In contrast, simulations of the patients' brains at three months post-stroke show striking attenuation in the signatures of brain criticality. While the curves of overall activity are just slightly decreased as compared to controls, the variability of activity, functional connectivity (FC), and entropy (H) are significantly decreased (Suppl. Material, Figs. S4-S8). The first cluster is significantly decreased in size, while the second cluster is significantly larger as compared to controls at multiple thresholds of activation (Fig. 3; Suppl. Material, Figs. S4-S8).

Crucially, the same criticality signatures reveal the recovery at one-year post-stroke. Indeed, the neural patterns in t_2

bioRxiv preprint doi: https://doi.org/10.1101/2020.12.17.423349; this version posted December 20, 2020. The copyright holder for this preprint (which was not certified by peer review) is the author/funder, who has granted bioRxiv a license to display the preprint in perpetuity. It is made available under aCC-BY-NC-ND 4.0 International license.

approach the corresponding controls' average, especially for S_2 and σ_A. Hence clusters of activity provide a dynamic estimate of the spread of neural activity, and a measure of integration-segregation in terms of coherent groups of active regions. Criticality alterations and their recovery were related to functional connectivity measures. There was a negative correlation between the decrease of the size of S_2 (towards the control's average) and the increase in whole-brain model FC (Fig. 6). Stroke-specific measures of disrupted FC, e.g. inter-hemispheric FC, were also related to S_2 size (Fig. 6).

Correlation between criticality and behavior

The role of criticality in behavior has been discussed in prior studies[75,76]. For instance, Palva et. al.[77] reported a strong correlation between scale-free neuronal avalanches and behavioral time-series in MEG/EEG data. The connection between human cognitive performance and criticality has also been investigated. Ezaki et. al provided empirical support that subjects with higher-IQ have neural dynamics closer to criticality than subjects with lower-IQ participants[78]. Our findings show for the first time that causal manipulations of brain activity, through lesions and recovery, modifies criticality in a significant behavioral manner. To measure behavioral impairment, we aggregated scores across multiple domains as computed in[47]. This index captures global disability and correlated with empirical measures of functional connectivity (Fig. 6). A normalization of criticality in terms of the size of the second cluster ($S_2(t_2-t_1)$) also correlated with the degree of behavioral recovery ($B(t_2 t_1)$, Fig. 6). Patients with greater recovery showed greater changes in S_2. Interestingly, the second-largest cluster of activity proved a better predictor of recovery than changes in model $FC_m(t_2-t_1)$ (Fig. 6) or entropy $H_m(t_2-t_1)$ (Suppl. Material, Fig. S12).

Anatomical connections supporting criticality and prediction of recovery

Specific connections in the brain at t_2 predicted with high accuracy, in a ridge regression model, criticality values (S_1 and S_2 size) at t_2. Moreover, surprisingly, connections at t_1 predicted changes of criticality between t_1 and t_2. Higher values and stronger criticality recovery were associated with visual connections, while lower values and weaker recovery were associated with DMN connections. Importantly, connections related to the recovery of criticality were not random but followed the normal topology of healthy functional connections. Accumulating evidence suggests that brain regions comprising the default-mode network (DMN) have a prominent role in maintaining resting-state networks[79] and in facilitating the spread of neural avalanches through the large-scale structural network[80].

In a recent review, Gollo et. al.[23] hypothesized that hub regions within the DMN represent a structural signature of near-critical dynamics. Our findings provide some support for this idea. Edges to/from DMN regions as well as networks sub-serving attention and executive control (cingulo-opercular and dorsal attention networks) predicted higher criticality values at t_2. And, regions comprising the visual and the DMN networks were clearly involved in the patients' criticality recovery from t_1 to t_2.

An increase in critical signatures from t_1 to t_2 must correspond to the recovery of structural (anatomical) connections, which is captured by diffusion-weighted imaging (DWI) and tractography. Changes in DWI and tractography may reflect a number of different homeostatic plasticity mechanisms, including structural plasticity in gray and white matter tracts, recovery of neural cells, remyelination, and rewiring. Whether long-range anatomical connectional changes support the recovery of function in stroke is not a well-explored issue. Longitudinal changes in micro- and macro-scale structural anatomy and physiology following experimentally induced strokes have been tracked in animals, mostly in the perilesional area[81]. However, there are also observations of long-range plasticity[82–84]. In humans, structural plasticity can be measured at the macro-scale level with diffusion MRI[85]. There is now convincing evidence in both humans and animals that learning through activity-dependent plasticity can modify white matter in healthy adults[86,87], and possibly in stroke patients[88–90].

Conclusions

In summary, our theoretical framework to model individual brain dynamics based on real structural connectivity networks suggests that patients affected by stroke present decreased levels of neural activity, decreased entropy, and decreased strength of the functional connections. All these factors contribute to an overall loss of criticality at three months post-stroke that recovers at twelve months, driven by white matter connections remodeling. Notably, our model contains only three parameters (r_1, r_2, and T), all set apriori without any fitting procedures. In conclusion, personalized whole-brain dynamical models poised at criticality track and predict stroke recovery at the level of the single patient, thereby opening promising paths for computational and translational neuroscience.

Methods

Stroke dataset

All data came from a large prospective longitudinal stroke study described in previous publications[33,47,53]. We provide here a brief description of the dataset and refer the reader to those articles for a more comprehensive description.

bioRxiv preprint doi: https://doi.org/10.1101/2020.12.17.423349; this version posted December 20, 2020. The copyright holder for this preprint (which was not certified by peer review) is the author/funder, who has granted bioRxiv a license to display the preprint in perpetuity. It is made available under aCC-BY-NC-ND 4.0 International license.

Clinical sample: The dataset includes 132 stroke patients at the sub-acute stage (2 weeks post-stroke). The inclusion/exclusion criteria were as follows: first symptomatic stroke, ischemic or hemorrhagic, and clinical evidence of any neurological deficit. We used data from the subset of 103 patients who returned for clinical and imaging assessments at three months post-stroke, as well as the data from the 88 patients who returned for 1 year post-stroke assessment (for details see Corbetta et al.[47]). The control group, formed by 28 individuals, was matched with the stroke sample for age, gender, and years of education. Data was collected twice in the healthy controls, 3 months apart. Stroke patients and healthy controls provided informed consent as approved by the Washington University Institutional Review Board Behavioral assessment.

The neuropsychological battery included 44 behavioral scores across five behavioral domains: language, memory, motor, attention, and visual function. These domains were chosen to represent a wide range of the most commonly identified deficits in people after a stroke.

MRI Acquisition

Patients were studied 2 weeks (mean = 13.4 d, SD = 4.8 d), 3 months (mean = 112.5 d, SD = 18.4 d), and 1 year (mean = 393.5 d, SD = 55.1 d) post-stroke. Diffusion data were obtained only at 3 months and 1 year. Controls were studied twice with an interval of 3 months. All imaging was performed using a Siemens 3T Tim-Trio scanner at WUSM and the standard 12-channel head coil. The MRI protocol included structural, functional, pulsed arterial spin labeling (PASL) and diffusion tensor scans. Structural scans included: (i) a sagittal T1-weighted MPRAGE (TR=1,950 ms, TE=2.26 ms, flip angle=90°, voxel size= $1.0 \times 1.0 \times 1.0$ mm); (ii) a transverse T2-weighted turbo spin echo (TR = 2,500 ms, TE = 435 ms, voxel size = $1.0 \times 1.0 \times 1.0$ mm); and (iii) sagittal fluid attenuated inversion recovery (FLAIR) (TR = 7,500 ms, TE = 326 ms, voxel size = $1.5 \times 1.5 \times 1.5$ mm). PASL acquisition parameters were: TR = 2,600 ms, TE = 13 ms, flip angle = 90°, bandwidth 2.232 kHz/Px, and FoV 220 mm; 120 volumes were acquired (322 s total), each containing 15 slices with slice thickness 6- and 23.7-mm gap. Resting state functional scans were acquired with a gradient echo EPI sequence (TR = 2,000 ms, TE = 27 ms, 32 contiguous 4-mm slices, 4×4 mm in-plane resolution) during which participants were instructed to fixate on a small cross in a low luminance environment. Six to eight resting state fMRI runs, each including 128 volumes (30 min total), were acquired. fMRI Data Preprocessing of fMRI data included: (i) compensation for asynchronous slice acquisition using sinc interpolation; (ii) elimination of odd/even slice intensity differences resulting from interleaved acquisition; (iii) whole brain intensity normalization to achieve a mode value of 1,000; (iv) removal of distortion using synthetic field map estimation and spatial realignment within and across fMRI runs; and (v) resampling to 3-mm cubic voxels in atlas space including realignment and atlas transformation in one resampling step. Cross-modal (e.g., T2 weighted to T1 weighted) image registration was accomplished by aligning image gradients. Cross-model image registration in patients was checked by comparing the optimized voxel similarity measure to the 97.5 percentile obtained in the control group. In some cases, structural images were substituted across sessions to improve the quality of registration.

Diffusion weighted imaging (DWI) included a total of 64 near-axial slices. We used a fully optimized acquisition sequence for tractography that provided isotropic ($2 \times 2 \times 2$ mm) resolution and coverage of the whole head with a posterior-anterior phase of acquisition. We set the echo time (TE) and the repetition time (TR) to 9.2 milliseconds and 9200 milliseconds, respectively. At each slice location, 4 images were acquired with no diffusion gradient applied. Additionally, 60 diffusion-weighted images were acquired, in which gradient directions were uniformly distributed on the hemisphere with electrostatic repulsion. The diffusion weighting was equal to a b-value of 1000 sec mm2. In order to optimize the contrast of acquisition, this sequence was repeated twice.

MRI and Lesion Analysis

Individual T1 MRI images were registered to the Montreal Neurological Institute brain using FSL (FMRIB Software Library) FNIRT (FMRIB nonlinear imaging registration tool). Lesions were manually segmented on individual structural MRI images (T1-weighted MPRAGE, T2-weighted spin echo images, and FLAIR images obtained 1–3 wk post-stroke) using the Analyze biomedical imaging software system (www.mayoclinic.org). Two board-certified neurologists (M.C. and Alexandre Carter) reviewed all segmentations. Special attention was given to distinguish lesion from cerebral spinal fluid (CSF), hemorrhage from surrounding edema, and to identify the degree of periventricular white matter damage present. In hemorrhagic strokes, edema was included in the lesion. A neurologist (M.C.) reviewed all segmentations a second time, paying special attention to the borders of the lesions and degree of white matter disease. The staff that was involved in segmenting or in reviewing the lesions was blind to the individual behavioral data. Atlas-registered segmented lesions ranged from 0.02 to 82.97 cm3 with a mean of 10.15 cm3 (SD = 13.94 cm3). Lesions were summed to display the number of patients with structural damage for each voxel.

Functional Connectivity (FC) Processing

FC processing followed previous work from the laboratory (see[32]), with the addition of surface projection and processing steps developed by the Human Connectome Project. First, data were passed through several additional preprocessing steps: (i)

bioRxiv preprint doi: https://doi.org/10.1101/2020.12.17.423349; this version posted December 20, 2020. The copyright holder for this preprint (which was not certified by peer review) is the author/funder, who has granted bioRxiv a license to display the preprint in perpetuity. It is made available under aCC-BY-NC-ND 4.0 International license.

regressors were computed based on Freesurfer segmentation; (ii) removal by regression of the following sources of spurious variance: (a) six parameters obtained by rigid body correction of head motion, (b) the signal averaged over the whole brain, signal from ventricles and CSF, and (d) signal from white matter; (ii) temporal filtering retaining frequencies in the 0.009–0.08Hz band; and (iii) frame censoring. The first four frames of each BOLD run were excluded. Frame censoring was computed using framewise displacement with a threshold of 0.5 mm. This frame-censoring criterion was uniformly applied to all R-fMRI data (patients and controls) before functional connectivity computations. Subjects with less than 120 usable BOLD frames were excluded (13 patients, 3 controls).

Surface generation and processing of functional data followed procedures similar to Glasser et al.[91], with additional consideration for cortical segmentation in stroke patients. First, anatomical surfaces were generated for each subject's T1 MRI using FreeSurfer automated segmentation[92]. This included brain extraction, segmentation, generation of white matter and pial surface, inflation of the surfaces to a sphere, and surface shape-based spherical registration to the subjects "native" surface to the fs average surface. Segmentations were manually checked for accuracy. For patients in whom the stroke disrupted automated segmentation, or registration, values within lesioned voxels were filled with normal atlas values before segmentation, and then masked immediately after (seven patients). The left and right hemispheres were then resampled to 164,000 vertices and registered to each other, and finally downsampled to 10,242 vertices each for projection of functional data. Following preprocessing of BOLD data, volumes were sampled to each subject's individual surface (between white matter and pial surface) using a ribbon-constrained sampling available in Connectome Workbench. Voxels with a high coefficient of variation (0.5 SDs above the mean coefficient of variation of all voxels in a 5-mm sigma Gaussian neighborhood) were excluded from volume to surface mapping[91]. Time courses were then smoothed along the 10,242 vertex surface using a 6-mm FWHM Gaussian kernel. Finally, time courses of all vertices within a parcel are averaged to make a parcelwise time series. We used a cortical surface parcellation generated by Gordon et al.[57]. The parcellation is based on R-fMRI boundary mapping and achieves full cortical coverage and optimal region homogeneity. The parcellation includes 324 regions of interest (159 left hemisphere, 165 right hemisphere). The original parcellation includes 333 regions, and all regions less than 20 vertices (approximately 50 mm2) were excluded. Notably, the parcellation was generated on young adults age 18–33 and is applied here to adults age 21–83.

Diffusion weighted imaging (DWI) processing

For each slice, diffusion-weighted data were simultaneously registered and corrected for subject motion and geometrical distortion adjusting the diffusion directions accordingly[93] (ExploreDTI http://www.exploredti.com). Spherical deconvolution was chosen to estimate multiple orientations in voxels containing different populations of crossing fibres[94–96]. The damped version of the Richardson-Lucy algorithm for spherical deconvolution[55] was calculated using Startrack (https://www.mr-startrack.com).

Algorithm parameters were chosen as previously described[54]. A fixed fibre response corresponding to a shape factor of $\alpha = 1.5 \times 10^{-3} mm^2/s$ was chosen[54]. Fibre orientation estimates were obtained by selecting the orientation corresponding to the peaks (local maxima) of the fibre orientation distribution (FOD) profiles. To exclude spurious local maxima, we applied both an absolute and a relative threshold on the FOD amplitude. A first "absolute" threshold was used to exclude intrinsically small local maxima due to noise or isotropic tissue. This threshold was set to 3 times the mean amplitude of a spherical FOD obtained from a grey matter isotropic voxel (and therefore also higher than an isotropic voxel in the cerebrospinal fluid). A second "relative" threshold of 10% of the maximum amplitude of the FOD was applied to remove the remaining local maxima with values higher than the absolute threshold[97].

Whole-brain tractography was performed selecting every brain voxel with at least one fibre orientation as a seed voxel. From these voxels, and for each fibre orientation, streamlines were propagated using Euler integration with a step size of 1 mm (as described in[54]). When entering a region with crossing white matter bundles, the algorithm followed the orientation vector of least curvature (as described in Schmahmann and Pandya[98]). Streamlines were halted when a voxel without fibre orientation was reached or when the curvature between two steps exceeded a threshold of 60°.

The whole-brain streamlines were registered to the standard MNI. For each patient, whole-brain streamline tractography was converted into streamline density volumes where the intensities corresponded to the number of streamlines crossing each voxel. A study-specific template of streamline density volumes was generated using the Greedy symmetric diffeomorphic normalization (GreedySyN) pipeline distributed with Advanced Normalization Tools[99] (ANTs, http://stnava.github.io/ANTs/). This provided an average template of the streamline density volumes for all subjects. The template was then co-registered with a standard 2 mm MNI152 template using flirt tool implemented in FSL to obtain a streamline density template in the MNI152 space. Finally, individual streamline density volumes were registered to the streamline density template in the MNI152 space template using ANTs GreedySyn. The same registration parameters were applied to the individual whole-brain streamline tractography using the trackmath tool distributed with the software package Tract Querier[100] using ANTs GreedySyn. This step produced a whole-brain streamline tractography in the standard MNI152 space.

Dissections were performed using trackvis[101] (http://trackvis.org). Regions of interest were derived from[57] and arranged 2

bioRxiv preprint doi: https://doi.org/10.1101/2020.12.17.423349; this version posted December 20, 2020. The copyright holder for this preprint (which was not certified by peer review) is the author/funder, who has granted bioRxiv a license to display the preprint in perpetuity. It is made available under aCC-BY-NC-ND 4.0 International license.

by 2 in order to select streamlines and build a connectivity matrix for each patient. We considered the number of streamlines existing between two regions as a surrogate of the strength of the connection. Although the number of streamlines is not precise enough for an accurate estimate of fibre strength[102], it is acceptable in the context of brain disconnection after a stroke[103,104].

Characterization of simulated brain activity

We have considered the following standard quantities to characterize the simulated brain activity:

- the mean network activity,

$$\langle A \rangle = \frac{1}{t_s} \sum_{t=1}^{t_s} A(t), \tag{2}$$

  where $A(t) = \sum_{i=1}^{N} s_i(t)/N$ is the instantaneous activity, N is the total number of nodes and t_s is the simulated total time;

- the standard deviation of $A(t)$,

$$\sigma_A = \sqrt{\frac{1}{t_s} \sum_{t=1}^{t_s} \big(A(t) - \langle A \rangle\big)^2}, \tag{3}$$

- the sizes of the averaged clusters, the largest $\langle S_1 \rangle$ and the second largest $\langle S_2 \rangle$. Clusters were defined as ensembles of nodes that are structurally connected to each other and simultaneously active.

Following our previous work[34], we set the model parameters to the following values, $r_1 = 2/N$ (with $N = 324$), $r_2 = r_1^{1/5}$, and we vary the activation threshold $T \in [0, 0.2]$. We updated the network states, starting from random configurations of A, I and R states, for a total of t_s time-steps. For each value of the threshold T we computed the state variables, $\langle S_1 \rangle$, $\langle S_2 \rangle$, $\langle A \rangle$ and σ_A. Throughout this study, unless stated otherwise, the final numerical results presented were averages over 50 initial random configurations. For computation of model data, we discarded the initial transient dynamics (first 100 time steps).

From the model output to BOLD signal

We have employed a standard procedure to transform model output in BOLD functional signals[34,60]. Accordingly, the node's activity, $s_i(t)$, is convolved with a canonical double-gamma hemodynamic response function (HRF),

$$x_i(t) = \int_0^{\infty} s_i(t-\tau) h(\tau) d\tau, \tag{4}$$

with,

$$h(\tau) = \left(\frac{\tau}{d_1}\right)^{a_1} e^{-\frac{\tau - d_1}{b_1}} - c \left(\frac{\tau}{d_2}\right)^{a_2} e^{-\frac{\tau - d_2}{b_2}}, \tag{5}$$

where $x_i(t)$ is the BOLD signal of the i-th node. The free parameters in (5) were fixed according to values found in[105], i.e., $d_i = a_i b_i$, $a_1 = 6$, $a_2 = 12$, $b_i = 0.9$, and $c = 0.35$. Finally, the BOLD time-series, $\mathbf{x}(t)$, were filtered with a zero lag finite impulse response band pass filter in the frequency range of $0.01 - 0.1\ Hz$.

From the generated BOLD signal we can finally extract the following quantities:

- the functional connectivity network (FC). In fact, the FC matrix FC_{ij} is defined through Pearson correlation:

$$\mathrm{FC}_{ij} = \frac{\langle x_i x_j \rangle - \langle x_i \rangle \langle x_j \rangle}{\sigma_i \sigma_j}, \tag{6}$$

  where $\sigma_i = \sqrt{\langle x_i^2 \rangle - \langle x_i \rangle^2}$ is the standard deviation and $\langle \cdot \rangle$ is the temporal average of the BOLD time series.

- the average of the functional connectivity:

$$\langle \mathrm{FC} \rangle = \frac{2}{N(N-1)} \sum_{i}^{N} \sum_{j>i}^{N} |\mathrm{FC}_{ij}|. \tag{7}$$

  From the above expression we observe that only the upper triangular elements of $|\mathrm{FC}|$ are considered in the average.

bioRxiv preprint doi: https://doi.org/10.1101/2020.12.17.423349; this version posted December 20, 2020. The copyright holder for this preprint (which was not certified by peer review) is the author/funder, who has granted bioRxiv a license to display the preprint in perpetuity. It is made available under aCC-BY-NC-ND 4.0 International license.

- the Shannon entropy:

$$H = -\sum_{i=1}^{m} p_i \log p_i / \log m, \tag{8}$$

where m is the number of bins used to construct the probability distribution function of the upper triangular elements of $|\mathrm{FC}|$. The normalization factor in the denominator, i.e., $\log m$, is the entropy of a uniform distribution, and it ensures that H is normalized between 0 and 1. Following[46], we partitioned our distributions, both for empirical and model generated data, with $m = 10$ bins. The higher the diversity of the functional connectivity matrix, the higher the entropy of that functional connectivity matrix.

- finally, we characterize the distance between any two given simulated neural quantities at t_1 and t_2 through the Euclidean distance:

$$d(t_1, t_2) = \sqrt{\sum_T (X_{t_2}(T) - X_{t_1}(T))^2}, \tag{9}$$

where $X_t(T)$ is a given neural pattern at time-point t and threshold T.

Mapping criticality to structural connectivity

The main aim of these analyses was to identify topographical patterns of the structural connectivity matrix (SC) that are related to criticality indexes through multivariate (machine learning) analyses. In our multivariate approach (also see Siegel et al.[33] and Salvalaggio et al.[63]), features of the individual SC matrices extracted by Principal Component Analysis (PCA) were used as multivariate predictors for a Ridge Regression (RR) model trained to predict patients' criticality values. RR differs from multiple linear regression because it uses L2-normalization to regularize model coefficients, so that unimportant features are automatically down weighted or eliminated, thereby preventing overfitting and improving generalization on test data[106]. The model weights W are computed as:

$$W = (X^T X + \lambda I)^{-1} X^T Y \tag{10}$$

where X is the set of predictors and Y is the outcome variable. The regularization term provides a constraint on the size of weights and it is controlled by parameter λ. A tuning procedure is necessary to find the appropriate value of λ. Importantly, this approach also allows to project predictive weights back to brain data in a very simple way[33,107]. Before applying RR, principal component analysis (PCA) was performed on the SC matrix to reduce the input dimensionality. The latter included $52,326$ edges, corresponding to all non-diagonal elements of one half of the symmetric SC matrix of 324 nodes/parcels. Principal Components (PCs) that explained 95% of the variance were retained and used as input for the RR model. All predictors (PC scores) and the outcome variable (criticality value) were z-normalized before applying RR. All RR models were trained and tested using a leave-one-(patient)-out cross validation (LOOCV) loop[108]. In each loop, the regularization coefficient λ was optimized by identifying a value between $\lambda = 10^{-5}$ and 10^5 (logarithmic steps) that minimized leave-one-out prediction error over the training set. Optimal weights were solved across the entire training set using gradient descent to minimize error for the ridge regression equation by varying λ. These model weights were then applied to the left-out patient to predict the criticality value. A prediction was generated for all patients in this way. Model accuracy was assessed using the coefficient of determination

$$R^2 = 1 - \frac{\sum (Y - Y')^2}{\sum (Y - \bar{Y})^2} \tag{11}$$

where Y are the measured criticality values, Y' are the predicted criticality values and $\bar{Y}$ is the mean of predicted criticality indexes. The statistical significance of all LOOCV results was assessed using permutation test. For each regression model, criticality scores were randomly permuted across subjects 10000 times, and the entire regression was carried out with each set of randomized labels. A P-value was calculated as the probability of observing the reported R^2 values by chance (number of permutation $R^2 >$ observed R^2)/(number of permutation). Finally, the RR weight matrix was averaged across all LOOCV loops to generate a single set of consensus weights. Statistical reliability of each consensus weight was assessed by comparing its distribution of values (throughout the LOOCV loops) to a null distribution (obtained from the null models generated for permutation testing) using a FDR corrected t-test. The final set of (statistically reliable) consensus weights was back projected to the brain to display a map of the most predictive structural connections.

bioRxiv preprint doi: https://doi.org/10.1101/2020.12.17.423349; this version posted December 20, 2020. The copyright holder for this preprint (which was not certified by peer review) is the author/funder, who has granted bioRxiv a license to display the preprint in perpetuity. It is made available under aCC-BY-NC-ND 4.0 International license.

References

1. J. Hesse and T. Gross. Self-organized criticality as a fundamental property of neural systems. Front. Syst. Neurosci. **8**, 166 (2014).
2. Paolo Massobrio, Lucilla de Arcangelis, Valentina Pasquale, Henrik J. Jensen and Dietmar Plenz. Criticality as a signature of healthy neural systems. Frontiers in Systems Neuroscience **15**, 22 (2015).
3. D. R. Chialvo. Emergent complex neural dynamics. Nat. Phys. **6**, 744 (2010).
4. Serena di Santo, Pablo Villegas, Raffaella Burioni, and Miguel A. Muñoz. Landau–Ginzburg theory of cortex dynamics: Scale-free avalanches emerge at the edge ofsynchronization. Proc. Natl. Acad. Sci. **115**, E1356-E1365 (2018).
5. Antonio J. Fontenele, Nivaldo A.P. de Vasconcelos, Thaís Feliciano, Leandro A.A. Aguiar, Carina Soares-Cunha, Bárbara Coimbra, Leonardo Dalla Porta, Sidarta Ribeiro, Ana João Rodrigues, Nuno Sousa, Pedro V. Carelli, and Mauro Copelli. Criticality between Cortical States. Phys. Rev. Lett. **122**, 208101 (2019).
6. Miguel A. Muñoz. Colloquium: Criticality and dynamical scaling in living systems. Rev. Mod. Phys. **90**, 031001 (2018).
7. Jorge Hidalgo, Jacopo Grilli, Samir Suweis, Miguel A. Muñoz, Jayanth R. Banavar and Amos Maritan. Information-based fitness and the emergence of criticality in living systems. Proc Natl Acad Sci USA **111** (28), 10095-10100 (2014).
8. Masa Tsuchiya, Alessandro Giuliani, Midori Hashimoto, Jekaterina Erenpreisa, Kenichi Yoshikawa. Self-Organizing Global Gene Expression Regulated through Criticality: Mechanism of the Cell-Fate Change. PLoS ONE **11**, e0167912 (2016).
9. Joseph W. Larkin, Xiaoling Zhai, Kaito Kikuchi, Samuel E. Redford, Arthur Prindle, Jintao Liu, Sacha Greenfield, Aleksandra M. Walczak, Jordi Garcia-Ojalvo, Andrew Mugler,and Gürol M. Süel. Signal Percolation within a Bacterial Community. Cell Systems **7**, 137-145 (2018).
10. A. Cavagna, A. Cimarelli, I. Giardina, G. Parisi, R. Santagati, F. Stefanini, M. Viale. Scale-free correlations in starling flocks. Proc. Natl. Acad. Sci. **107**, 11865-11870 (2010).
11. J. M. Beggs and D. Plenz. Neuronal avalanches in neocortical circuits. J. Neurosci. **23**, 11167 (2003).
12. E. D. Gireesh and D. Plenz. Neuronal avalanches organize as nested theta and beta/gamma oscillations during development of cortical layer 2/3. Proc. Natl. Acad. Sci. USA **105**, 7576–7581 (2008).
13. T. Petermann et al. Spontaneous cortical activity in awake monkeys composed of neuronal avalanches. Proc. Natl. Acad. Sci. USA **106**, 15921–15926 (2009).
14. Enzo Tagliazucchi, Pablo Balenzuela, Daniel Fraiman and Dante R. Chialvo. Criticality in large-scale brain fMRI dynamics unveiled by a novel point process analysis. Frontiers in Physiology **3**, 15 (2012).
15. K. Linkenkaer-Hansen, V.V. Nikulin, J.M. Palva, and R.J. Ilmoniemi. Long-range temporal correlations and scaling behavior in human brain oscillations. J. Neurosci. **21**, 1370 (2001).
16. Paul Expert, Renaud Lambiotte, Dante R. Chialvo, Kim Christensen, Henrik Jeldtoft Jensen, David J. Sharp and Federico Turkheimer. Self-similar correlation function in brain resting-state functional magnetic resonance imaging. J. R. Soc. Interface **8**, 472–479 (2011).
17. Daniel Fraiman and Dante R. Chialvo. What kind of noise is brain noise: anomalous scaling behavior of the resting brain activity fluctuations. Frontiers in Physiology **3**, 307 (2012).
18. M.G. Kitzbichler, M.L. Smith, S.R. Christensen and E. Bullmore. Broadband criticality of human brain network synchronization. PLoS Comput. Biol. **5**, e1000314 (2009).
19. G.C. Van Orden, J.G. Holden, and M.T. Turvey. Human cognition and $1/f$ scaling. J. Exp. Psychol. Gen. **134**, 117–123 (2005).
20. B. Vázquez-Rodríguez et al. Stochastic resonance at criticality in a network model of the human cortex. Sci. Reports **7**, 13020 (2017).
21. C. Haldeman and J. Beggs. Critical branching captures activity in living neural networks and maximizes the number of metastable states. Phys. Rev. Lett. **94**, 058101 (2005).
22. E. Schneidman, M.J. Berry, R. Segev, and W. Bialek. Weak pairwise correlations imply strongly correlated network states in a neural population. Nature **440**, 1007–1012 (2006).
23. Luca Cocchi, Leonardo L. Gollo, Andrew Zalesky,Michael Breakspear. Criticality in the brain: A synthesis of neurobiology, models and cognition. Progress in Neurobiology **158**, 132-152 (2017).

bioRxiv preprint doi: https://doi.org/10.1101/2020.12.17.423349; this version posted December 20, 2020. The copyright holder for this preprint (which was not certified by peer review) is the author/funder, who has granted bioRxiv a license to display the preprint in perpetuity. It is made available under aCC-BY-NC-ND 4.0 International license.

24. Christian Meisel, Alexander Storch, Susanne Hellmeyer-Elgner, Ed Bullmore and Thilo Gross. Failure of adaptive self-organized criticality during epileptic seizure attacks. PLoS Comp. Biol. **8**, e10002312 (2012).

25. Christian Meisel. Antiepileptic drugs induce subcritical dynamics in human cortical networks. Proc. Natl. Acad. Sci. **117**, 11118-11125 (2020).

26. V. Priesemann, M. Valderrama, M. Wibral, and M. Le Van Quyen. Neuronal avalanches differ from wakefulness to deep sleep: evidence from intracranial depth recordings in humans. PLoS Comp. Biol. **9**(3), e1002985 (2013).

27. G. Scott et al. Voltage imaging of waking mouse cortex reveals emergence of critical neuronal dynamics. J. Neurosci. **34**, 16611–16620 (2014).

28. Christian Meisel, Eckehard Olbrich, Oren Shriki, and Peter Achermann. Fading Signatures of Critical Brain Dynamics during Sustained Wakefulness in Humans. The Journal of Neuroscience **33**, 17363–17372 (2013).

29. Heonsoo Lee, Daniel Golkowski, Denis Jordan, Sebastian Berger, Rüdiger Ilg, Joseph Lee, George A. Mashour, UnCheol Lee, the ReCCognition Study Group. Relationship of critical dynamics, functional connectivity, and states of consciousness in large-scale human brain networks. NeuroImage **188**, 228-238 (2019).

30. Enzo Tagliazucchi, Dante R. Chialvo, Michael Siniatchkin, Enrico Amico, Jean-Francois Brichant, Vincent Bonhomme, Quentin Noirhomme, Helmut Laufs and Steven Laureys. Large-scale signatures of unconsciousness are consistent with a departure from critical dynamics. J. R. Soc. Interface **13**, 20151027 (2016).

31. Lili Jiang, Danyang Sui, Kaini Qiao, Hao-Ming Dong, Luonan Chen and Ying Han. Impaired Functional Criticality of Human Brain during Alzheimer's Disease Progression. Sci. Rep. **8**, 1324 (2018).

32. Joshua S. Siegel, Benjamin A. Seitzman, Lenny E. Ramsey, Mario Ortega, Evan M. Gordon, Nico U.F. Dosenbach, Steven E. Petersen, Gordon L. Shulman, Maurizio Corbetta. Re-emergence of modular brain networks in stroke recovery. Cortex **101**, 44-59 (2018).

33. Joshua Sarfaty Siegel, Lenny E. Ramsey, Abraham Z. Snyder, Nicholas V. Metcalf, Ravi V. Chacko, Kilian Weinberger, Antonello Baldassarre, Carl D. Hacker, Gordon L. Shulman, and Maurizio Corbetta. Disruptions of network connectivity predict impairment in multiple behavioral domains after stroke. Proc. Natl. Acad. Sci. USA **113** (30), E4367-E4376 (2016).

34. Rodrigo P. Rocha, Loren Koçillari, Samir Suweis, Maurizio Corbetta and Amos Maritan. Homeostatic plasticity and emergence of functional networks in a whole-brain model at criticality. Sci. Rep. **8**, 15682 (2018).

35. Christopher J. Honey and Olaf Sporns. Dynamical consequences of lesions in cortical networks. Human Brain Mapping **29**, 802-809 (2008).

36. Jeffrey Alstott, Michael Breakspear, Patric Hagmann, Leila Cammoun and Olaf Sporns. Modeling the impact of lesions in the human brain. PLoS Comp. Biol. **5**, e10000408 (2009).

37. Caterina Gratton, Emi M. Nomura, Fernando Pérez, and Mark D'Esposito. Focal brain lesions to critical locations cause widespread disruption of the modular organization of the brain. J. Cogn. Neurosci. **24**, 1275-1285 (2012).

38. Joana Cabral, Etienne Hugues, Morten L. Kringelbach, and Gustavo Deco. Modeling the outcome of structural disconnection on resting-state functional connectivity. NeuroImage **62**, 1342-1353 (2012).

39. František Váša, Murray Shanahan, Peter J. Hellyer, Gregory Scott, Joana Cabral, and Robert Leech. Effects of lesions on synchrony and metastability in cortical networks. NeuroImage **118**, 456-467 (2015).

40. Peter J. Hellyer, Gregory Scott, Murray Shanahan, David J. Sharp, and Robert Leech. Cognitive flexibility through metastable neural dynamics is disrupted by damage to the structural connectome. The Journal of Neuroscience **35**, 9050-9063 (2015).

41. Anirudh Vattikonda, Bapi Raju Surampudi, Arpan Banerjee, Gustavo Deco, and Dipanjan Roy. Does the regulation of local excitation-inhibition balance aid in recovery of functional connectivity? A computational account. NeuroImage **136**, 57-67 (2016).

42. Maria Inez Falcon, Jeffrey D. Riley, Viktor Jirsa, Anthony R. Mclntosh, E. Elinor Chen, and Ana Solodkin. Functional mechanisms of recovery after chronic stroke: modeling with the virtual brain. eNeuro **3**, e0158-15.2016 (2016).

43. Hans-Otto Karnath Christoph Sperber, and Christopher Rordern. Mapping human brain lesions and their functional consequences. NeuroImage **165**, 180-189 (2018).

44. Ariel Haimovici, Pablo Balenzuela, and Enzo Tagliazucchi. Dynamical signatures of structural connectivity damage to a model of the brain posed at criticality. Brain connectivity **6**, 759-771 (2016).

bioRxiv preprint doi: https://doi.org/10.1101/2020.12.17.423349; this version posted December 20, 2020. The copyright holder for this preprint (which was not certified by peer review) is the author/funder, who has granted bioRxiv a license to display the preprint in perpetuity. It is made available under aCC-BY-NC-ND 4.0 International license.

45. Mohit H. Adhikari, Carl D. Hacker, Josh S. Siegel, Alessandra Griffa, Patric Hagmann, Gustavo Deco, and Maurizio Corbetta. Decreased integration and information capacity in stroke measured by whole brain models of resting state activity. Brain **140**, 1068–1085 (2017).

46. Victor M. Saenger, Adrián Ponce-Alvarez, Mohit Adhikari, Patric Hagmann, Gustavo Deco, and Maurizio Corbetta. Linking entropy at rest with the underlying structural connectivity in the healthy and lesioned brain. Cerebral Cortex **28**, 2948–2958 (2017).

47. Maurizio Corbetta, Lenny Ramsey, Alicia Callejas, Antonello Baldassarre, Carl D. Hacker, Joshua S. Siegel, Serguei V. Astafiev, Jennifer Rengachary, Kristina Zinn, Catherine E. Lang, Lisa Tabor Connor, Robert Fucetola, Michael Strube, Alex R. Carter, and Gordon L. Shulman. Common Behavioral Clusters and Subcortical Anatomy in Stroke. Neuron **85**, 927–941 (2015).

48. Joseph C.Griffis, Nicholas V.Metcalf, Maurizio Corbetta, Gordon L. Shulman. Damage to the shortest structural paths between brain regions is associated with disruptions of resting-state functional connectivity after stroke. NeuroImage **210**, 116589 (2020).

49. Joseph C. Griffis, Nicholas V. Metcalf, Maurizio Corbetta and Gordon L. Shulman. Structural Disconnections Explain Brain Network Dysfunction after Stroke. Cell Reports **28**, 2527-2540 (2019).

50. Antonello Baldassarre , Lenny Ramsey, Carl L. Hacker, Alicia Callejas, Serguei V. Astafiev, Nicholas V. Metcalf, Kristi Zinn, Jennifer Rengachary, Abraham Z. Snyder, Alex R. Carter, Gordon L. Shulman, Maurizio Corbetta. Large-scale changes in network interactions as a physiological signature of spatial neglect. Brain **137**, 3267-3283 (2014).

51. Maurizio Corbetta, Joshua S.Siegel, Gordon L. Shulman. On the low dimensionality of behavioral deficits and alterations of brain network connectivity after focal injury. Cortex **107**, 229-237 (2018).

52. Emi M. Nomura, Caterina Gratton, Renee M. Visser, Andrew Kayser, Fernando Perez, and Mark D'Esposito. Double dissociation of two cognitive control networks in patients with focal brain lesions. Proc. Natl. Acad. Sci. USA **107**, 12017-12022 (2010).

53. L.E. Ramsey, J.S. Siegel, C.E. Lang, M. Strube, G.L. Shulman and M. Corbetta. Behavioural clusters and predictors of performance during recovery from stroke. Nat. Hum. Behav. **1**, 0038 (2017).

54. Flavio Dell'Acqua, Andrew Simmons, Steven C.R. Williams, Marco Catani. Can spherical deconvolution provide more information than fiber orientations? Hindrance modulated orientational anisotropy, a true-tract specific index to characterize white matter diffusion. Human Brain Mapping **34**, 2464-2483 (2013).

55. Flavio Dell'Acqua, Paola Scifo, Giovanna Rizzo, Marco Catani, Andrew Simmons, Giuseppe Scotti, Ferruccio Fazio. A Modified Damped Richardson Lucy Algorithm to Reduce Isotropic Back-ground Effects in Spherical Deconvolution. NeuroImage **49**, 1446-1458 (2010).

56. Patric Hagmann, Leila Cammoun, Xavier Gigandet, Reto Meuli, Christopher J. Honey, Van J. Wedeen, Olaf Sporns. Mapping the Structural Core of Human Cerebral Cortex. PLoS Biol 6(7): e159.

57. Evan M Gordon, Timothy O Laumann, Babatunde Adeyemo, Jeremy F Huckins, William M Kelley , Steven E Petersen. Generation and Evaluation of a Cortical Area Parcellation From Resting-State Correlations. Cerebral Cortex **26**, 288-303 (2016).

58. A Haimovici, E Tagliazucchi, P Balenzuela, DR Chialvo. Brain organization into resting state networks emerges at criticality on a model of the human connectome. Phys. Rev. Lett. **110**, 178101 (2013).

59. Géza Ódor. Critical dynamics on a large human open connectome network. Phys. Rev. E **94**, 062411 (2016).

60. Ariel Haimovici, Enzo Tagliazucchi, Pablo Balenzuela, and Dante R. Chialvo. Brain organization into resting state networks emerges at criticality on a model of the human connectome. Phys. Rev. Lett. **110**, 178101 (2013).

61. Mahdi Zarepour, Juan I. Perotti, Orlando V. Billoni, Dante R. Chialvo, and Sergio A. Canna. Universal and nonuniversal neural dynamics on small world connectomes:A finite-size scaling analysis. Phys. Rev. E **100**, 052138 (2019).

62. Gustavo Deco, Giulio Tononi, Melanie Boly and Morten L. Kringelbach. Rethinking segregation and integration: contributions of whole-brain modelling. Nature Reviews Neuroscience **16**, 430-439 (2015).

63. Alessandro Salvalaggio, Michele De Filippo De Grazia, Marco Zorzi, Michel Thiebaut de Schotten, Maurizio Corbetta. Post-stroke deficit prediction from lesion and indirect structural and functional disconnection. Brain **143**, 2173-2188 (2020).

bioRxiv preprint doi: https://doi.org/10.1101/2020.12.17.423349; this version posted December 20, 2020. The copyright holder for this preprint (which was not certified by peer review) is the author/funder, who has granted bioRxiv a license to display the preprint in perpetuity. It is made available under aCC-BY-NC-ND 4.0 International license.

64. Alex R. Carter, Serguei V. Astafiev, Catherine E. Lang, Lisa T. Connor, Jennifer Rengachary, Michael J. Strube, Daniel L. W. Pope, Gordon L. Shulman, Maurizio Corbetta. Resting interhemispheric functional magnetic resonance imaging connectivity predicts performance after stroke. Ann. Neurol. **67**, 365–375 (2010).

65. B. J. He, A. Z. Snyder, J. L. Vincent, A. Epstein, G. L. Shulman, and M. Corbetta. Breakdown of functional connectivity in frontoparietal networks underlies behavioral deficits in spatial neglect. Neuron **53**, 905-918 (2007).

66. J. M. Greenberg and S. P. Hastings. Spatial Patterns for Discrete Models of Diffusion in Excitable Media. SIAM Journal on Applied Mathematics **34** (3), 515–523 (1978).

67. Gustavo Deco, Adrián Ponce-Alvarez, Patric Hagmann, Gian Luca Romani, Dante Mantini and Maurizio Corbetta. How Local Excitation–Inhibition Ratio Impacts the Whole Brain Dynamics. The Journal of Neuroscience **34**, 7886 (2014).

68. Peter J. Hellyer, Barbara Jachs, Claudia Clopath, Robert Leech. Local inhibitory plasticity tunes macroscopic brain dynamics and allows the emergence of functional brain networks. NeuroImage **124**, 85 (2015).

69. Romesh G. Abeysuriya, Jonathan Hadida, Stamatios N. Sotiropoulos, Saad Jbabdi, Robert Becker, Benjamin A. E. Hunt, Matthew J. Brookes, Mark W. Woolrich. A biophysical model of dynamic balancing of excitation and inhibition in fast oscillatory large-scale networks.

70. F.C. Yeh, S. Panesar, D. Fernandes, A. Meola, M. Yoshino, J.C. Fernandez-Miranda, J.M. Vettel, and T. Verstynen. Population-averaged atlas of the macroscale human structural connectome and its network topology. NeuroImage **178**, 57-68 (2018).

71. Ryan N. Gutenkunst, Joshua J. Waterfall, Fergal P. Casey, Kevin S. Brown, Christopher R. Myers, James P. Sethna. Universally Sloppy Parameter Sensitivities in Systems Biology Models. Plos Comput Biol 3: e189 (2007).

72. L. S. Katafygiotis and J. L. Beck. Updating Models and Their Uncertainties. II Model Identifiability. Journal of Engineering Mechanics **124**, 463-467 (1998).

73. Douglas M. Hawkins. The problem of overfitting. J. Chem. Inf. Comput. Sci. **44**, 1-12 (2004).

74. Benjamin B. Machta, Ricky Chachra, Mark K. Transtrum, James P. Sethna. Parameter Space Compression Underlies Emergent Theories and Predictive Models. Science **342**, 604-607 (2013).

75. J. Kelso, S. Bressler, S. Buchanan, G. DeGuzman, M. Ding, A. Fuchs, T. Holroyd. A phase transition in human brain and behavior. Physics Letters A **169**, 134-144 (1992).

76. V. K. Jirsa, R. Friedrich, H. Haken, J.S. Kelso. A theoretical model of phase transitions in the human brain. Biological cybernetics **71**, 27-35 (1994).

77. J.M. Palva, A. Zhigalov, J. Hirvonen, O. Korhonen, K. Linkenkaer-Hansen, S. Palva. Neuronal long-range temporal correlations and avalanche dynamics are correlated with behavioral scaling laws. Proc. Natl. Acad. Sci. **110**, 3585-3590 (2013).

78. Takahiro Ezaki, Elohim Fonseca dos Reis, Takamitsu Watanabe, Michiko Sakaki and Naoki Masuda. Closer to critical resting-state neural dynamics in individuals with higher fluid intelligence. Cummunications Biology **3**, 52 (2020).

79. Leonardo L. Gollo, Andrew Zalesky, R. Matthew Hutchison, Martijn van den Heuvel and Michael Breakspear. Dwelling quietly in the rich club: brain network determinants of slow cortical fluctuations. Phil. Trans. R. Soc. B **370**, 20140165 (2015)

80. Bratislav Mišić, Richard F.Betzel, Azadeh Nematzadeh, Joaquin Goñi, Alessandra Griffa, Patric Hagmann, Alessandro Flammini, Yong-Yeol Ahn, Olaf Sporns. Cooperative and Competitive Spreading Dynamics on the Human Connectome. Neuron **86**, 1518-1529 (2015).

81. S. Thomas Carmichael, Balachandar Kathirvelu, Catherine A Schweppe, Esther H Nie. Molecular, cellular and functional events in axonal sprouting after stroke. Experimental Neurology **287**, 384-394 (2017).

82. Numa Dancause, Scott Barbay, Shawn B. Frost, Erik J. Plautz, Daofen Chen, Elena V. Zoubina, Ann M. Stowe and Randolph J. Nudo. Extensive Cortical Rewiring after Brain Injury. Journal of Neuroscience **25**, 10167-10179 (2005).

83. S. Thomas Carmichael and Marie-Françoise Chesselet. Synchronous Neuronal Activity Is a Signal for Axonal Sprouting after Cortical Lesions in the Adult. Journal of Neuroscience **22**, 6062-6070 (2002).

84. Michel RT Sinke, Willem M Otte, Maurits PA van Meer, Annette van der Toorn and Rick M Dijkhuizen. Modified structural network backbone in the contralesional hemisphere chronically after stroke in rat brain. Journal Cereb Blood Flow Metab. **38**, 1642-1653 (2018).

bioRxiv preprint doi: https://doi.org/10.1101/2020.12.17.423349; this version posted December 20, 2020. The copyright holder for this preprint (which was not certified by peer review) is the author/funder, who has granted bioRxiv a license to display the preprint in perpetuity. It is made available under aCC-BY-NC-ND 4.0 International license.

85. Yaniv Assaf, Heidi Johansen-Berg, Michel Thiebaut de Schotten. The role of diffusion MRI in neuroscience. NMR in Biomedicine **32**, e3762 (2017).

86. R. Douglas Fields. A new mechanism of nervous system plasticity: activity-dependent myelination. Nature Reviews Neuroscience **16**, 756-767 (2015).

87. Cassandra Sampaio-Baptista, Zeena-Britt Sanders, and Heidi Johansen-Berg. Structural Plasticity in Adulthood with Motor Learning and Stroke Rehabilitation. Annual Review of Neuroscience **41**, 25-40 (2018).

88. Cathy M. Stinear, P. Alan Barber, Peter R. Smale, James P. Coxon, Melanie K. Fleming, Winston D. Byblow. Functional potential in chronic stroke patients depends on corticospinal tract integrity. Brain **130**, 170-180 (2007).

89. Roza M. Umarova, Lena Beume, Marco Reisert, Christoph P. Kaller, Stefan Klöppel, Irina Mader, Volkmar Glauche, Valerij G. Kiselev, Marco Catani, Cornelius Weiller. Distinct white matter alterations following severe stroke Longitudinal DTI study in neglect. Neurology 88, 1546-1555 (2017).

90. Thomas M. H. Hope, Alex P. Leff, Susan Prejawa, Rachel Bruce, Zula Haigh, Louise Lim, Sue Ramsden, Marion Oberhuber, Philipp Ludersdorfer, Jenny Crinion, Mohamed L. Seghier, Cathy J. Price. Right hemisphere structural adaptation and changing language skills years after left hemisphere stroke. Brain **140**, 1718-1728 (2017).

91. Glasser MF, Sotiropoulos SN, Wilson JA, Coalson TS, Fischl B, Andersson JL, et al. (2013). The minimal preprocessing pipelines for the Human Connectome Project. Neuroimage, 80, 105–124. 10.1016/j.neuroimage.2013.04.127.

92. Fischl B, Sereno MI, Tootell RBH, and Dale AM (1999). High-resolution intersubject averaging and a coordinate system for the cortical surface. Human Brain Mapping, 8(4), 272–284.

93. A. Leemans and D. K. Jones. The B-matrix must be rotated when correcting for subject motion in DTI data. Magnetic Resonance in Medecine 61(6): 1336-1349 (2009).

94. Daniel C. Alexander. An introduction to computational diffusion MRI: the diffusion tensor and beyond. Visualization and Processing of Tensor Fields. Berlin, Springer: 83-106 (2006).

95. Adam W. Anderson. Measurement of fiber orientation distributions using high angular resolution diffusion imaging. Magnetic resonance in medicine : official journal of the Society of Magnetic Resonance in Medicine / Society of Magnetic Resonance in Medicine 54(5): 1194-1206 (2005).

96. J. Donald Tournier, Fernando Calamante, David G.Gadian and Alan Connelly. Direct estimation of the fiber orientation density function from diffusion-weighted MRI data using spherical deconvolution. NeuroImage 23, 1176-1185 (2004).

97. F. Dell'Acqua, J. Coward, A. Simmons, D. Murphy, S. Williams, and M. Catani. Mapping Crossing Fibres of the Human Brain with Spherical Deconvolution: Towards an Atlas for Clinico-Anatomical Correlation Studies. Proceedings of the International Society of Magnetic Resonance Medicine 17: 3562 (2009).

98. J. D. Schmahmann et al. Association fibre pathways of the brain: parallel observations from diffusion spectrum imaging and autoradiography. Brain 130: 630-653 (2007).

99. B. B. Avants et al. A reproducible evaluation of ANTs similarity metric performance in brain image registration. Neuroimage 54(3): 2033-2044 (2011).

100. D. Wassermann et al. The white matter query language: a novel approach for describing human white matter anatomy. Brain Struct Funct 221(9): 4705-4721 (2016). studies with complete virtual "in vivo" tractography dissection. Cereb Cortex 24(3): 691-706 (2014).

101. V. J. Wedeen et al. Diffusion spectrum magnetic resonance imaging (DSI) tractography of crossing fibers. Neuroimage 41(4): 1267-1277 (2008).

102. D. K. Jones and M. Cercignani. Twenty-five pitfalls in the analysis of diffusion MRI data. NMR Biomed 23(7): 803-820 (2010).

103. S. J. Forkel et al. Anatomical predictors of aphasia recovery: a tractography study of bilateral perisylvian language networks. Brain 137: 2027-2039 (2014).

104. M. Thiebaut de Schotten et al. Damage to white matter pathways in subacute and chronic spatial neglect: a group study and 2 single-case

105. G. Glover. Deconvolution of Impulse Response in Event-Related BOLD fMRI. NeuroImage **9**, 416–429 (1999).

106. Le Cessie S, Van Houwelingen J C. Ridge Estimators in Logistic Regression. Journal of the Royal Statistical Society 1992. Series C (Applied Statistics), Vol. 41, No. 1, pp. 191-201.

bioRxiv preprint doi: https://doi.org/10.1101/2020.12.17.423349; this version posted December 20, 2020. The copyright holder for this preprint (which was not certified by peer review) is the author/funder, who has granted bioRxiv a license to display the preprint in perpetuity. It is made available under aCC-BY-NC-ND 4.0 International license.

107. Phan TG, Chen J, Donnan G, Srikanth V, Wood A, Reutens DC. Development of a new tool to correlate stroke outcome with infarct topography: A proof-of-concept study. Neuroimage 2010 49(1):127–133.

108. Golland P, Fischl B. Permutation tests for classification: Towards statistical significance in image-based studies. Information Processing in Medical Imaging, eds Taylor C, Noble JA, Lecture Notes in Computer Science (Springer, Berlin) 2003, pp 330–341.

Acknowledgements

R.P.R. was supported by the Research, Innovation and Dissemination Center for Neuromathematics (FAPESP Grant No. 2018/08609-8). M.D.F. and M.Z. were supported by the Italian Ministry of Health under Grant Number RF-2013-02359306.

Author contributions

R.P.R., S.S., and M.C. conceived the study. M.T.S. performed the pre-processing of structural connectivity data. R.P.R. performed the research. R.P.R. and L.K. analized the data. M.F.G. and M.Z. performed the Ridge Regression computation. R.P.R. wrote the first draft of the manuscript and all authors reviewed the manuscript.

Competing financial interests

The authors declare no competing financial interests.